Thesis

4D MRI reconstruction, modeling and disease analysis of thoracoabdominal organs

July 2015

Windra Swastika

Department of Medical System, Artificial Systems Science,
Graduate School of Engineering
Chiba University

千葉大学審査学位論文

胸腹部臓器の４次元 MR 画像構成、モデリングおよび疾患解析

2015 年 07 月

Windra Swastika

千葉大学大学院　工学研究科
人工システム科学専攻　メディカルシステムコース
羽石研究室

SUMMARY

4-dimensional magnetic resonance imaging (4D-MRI) is an imaging technique that reconstructs a 3D MRI with time series from a set of time sequential images of 2D MR. One of the advantages of 4D medical imaging over 3D medical imaging is that the anatomic motion and organ deformation caused by respiratory motion can be clearly observed. Retrospective method is a common method that has been widely use to reconstruct 4D imaging. However, it requires long acquisition time. A prospective method to reconstruct 4D-MRI especially for thoracoabdominal organ was proposed in this thesis. The main purpose is to shorten the acquisition time while maintaining the quality. Although the prospective method is tested only in simulations using previously fully acquired data sets, it is successfully reduced time acquisition of data slices by 75.7% and 82.1% for the volunteers and patients. A clinical application of 4D-MRI is also discussed in this thesis. The diaphragm motion from 4D-MRI of 8 chronic obstructive pulmonary disease (COPD) patients and 8 healthy volunteers were extracted. The displacements of the diaphragm were normalized and compared between COPD patients and healthy volunteers. The average of the normalized displacement of COPD patients was found to be smaller compared to healthy volunteers. Using the same diaphragm motion, we also generated inhalation phase length map that can be used to locate paradoxical motion of the diaphragm, which is one of the characteristics of COPD.

CONTENTS

LIST OF FIGURES

LIST OF TABLES

1

INTRODUCTION

1.1. Research on 4D imaging

Study of four-dimensional (4D) medical imaging of thoracoabdominal organs has been increasingly applied in radiotherapy treatment planning [1] [2]. One of the advantages of 4D medical imaging over 3D medical imaging is that the anatomic motion and organ deformation caused by respiratory motion can be clearly observed. This leads to better planning and delivery of radiotherapy. There are two common imaging modalities to reconstruct 4D medical imaging: computed tomography (CT) and magnetic resonance image (MRI). Table 1.1 shows the comparison of the common approach of each modality.

Table 1. 1. Common approach of 4D imaging using CT and MRI

4D-CT reconstruction [3] [4] [5] [6] [7]	**4D-MRI reconstruction** [8] [9] [10] [11] [12]
Prospective gating: - Requires a predetermined gating window **Retrospective gating:** - Obtaining images in all breathing phases	**Common approach:** - Obtain 2D-MR images to cover volume and respiratory phases from inhalation to exhalation phases. - Sorted based on the respiratory phase.
Con: - Image acquisition uses high-energy radiation	**Con:** - Long acquisition times because a large number of 2D images must be acquired

Early reports on using 4D-CT acquisition may be found in the literature [3] [4] [5]. There are two standard ways to carry out 4D-CT: prospective gating and retrospective gating [3] [4] [5] [6] [7]. Prospective gating requires a predetermined gating window in specific breathing phases. Images are taken only when the respiratory phase is within the gating window. The process is repeated until volume of interest in a certain respiratory phase is fully covered. On the other hand, retrospective gating 4D-CT requires obtaining images in all breathing phases without a gating window and covering volume of interest. Those images are then synchronized according to their respective respiratory phases and locations using a separate signal that represents its breathing phase.

Another common imaging modality used to reconstruct 4D medical imaging of thoracoabdominal organs is magnetic resonance imaging (MRI). Reconstruction of 4D-MR images has been less investigated compared to 4D-CT, which is well-established. Several studies have proposed reconstruction of 4D-MR images using time-sequential 2D-MR images [8] [9] [10] [11] [12]. A common approach for

reconstruction of 4D-MR images is using 2D-MR images to cover both the volume of the respiratory organ and the volume of the respiratory phases from inhalation to exhalation phases. The 2D-MR images are then retrospectively sorted based on the obtained respiratory phase to reconstruct the 4D-MR images (i.e. retrospective 4D-MRI).

Although the results of the reconstruction usually have good image quality, retrospective 4D-MRI requires long acquisition times because a large number of 2D images must be acquired for the purposes of sorting and volume construction. For example, von Siebenthal et al. [8] developed a retrospective 4D-MRI process using a dedicated navigator slice at a fixed position that consists of 2D-MR image sequences. The purpose of the navigator slice is to determine the phase of a certain data frame for image sorting before reconstructing the complete 3D images in a whole breathing cycle. Although the data frame 2D-MR images are acquired using fast 2D imaging (175ms/frame), the total acquisition time is about an hour. An additional 1.5-3 hours are required for the purpose of determining the frame similarity by tracking the region of interest (ROI) over 3000-7000 navigator images. Such retrospective 4D-MRI consists of many breathing cycles and captures the irregularity of respiration as well.

One navigator-based method that is used for 4D-MRI reconstruction was proposed by Tokuda et al [9]. This method was designed to acquire a series of 3D images that cover the whole range of respiratory organs by using the gating method. Instead of using one gating window, Tokuda et al used several bins (gating windows) to segment respiratory signals into several partitions. Since the purpose of this method is to obtain real-time tracking of 4D-MRI, complex hardware integration that used an A/D converter, RF pulse, and personal computer with MR scanner is required.

1.2. 4D-MRI reconstruction using intersection profile method

A hardware-independent method to reconstruct a robust and high-quality 4D-MR image consisting one breathing cycle from a temporal sequence of 2D-MR images has been developed previously [13]. This is a navigator-based method called the intersection profile method. Time sequential 2D-MR images in the sagittal plane which functions as the navigator slice are obtained first for a long time so as to include many respiration cycles, typically 3 min. Data slices (time sequential 2D-MR images in the coronal plane) are then obtained from the front (anterior) to back (posterior) body positions for 1 min for each slice position. Several spatio-temporal patterns from both the navigator slice and data slices are extracted at their intersection location to obtain the respiratory patterns. The 4D-MRI reconstruction is done by combining a proper respiratory pattern from each data slice that has the highest similarity to the corresponding navigator slice. The detail of the method is discussed in the following sections.

1.2.1. Materials

The MR images were acquired using 1.5T INTERA ACHIVA nova-dual (Philips Medical Systems) whole-body scanner with a 16ch SENSE TORSO XL coil. A 2D balanced FFE sequence was used. The imaging parameters were as follows: SENSE factor, 2.2; flip angle, 45^{o}; TR, 2.2ms; TE, 0.9ms; FOV, 384mm; in-plane resolution, 256x256 pixels and 1.5x1.5mm^2; slice thickness, 7.5mm; slice gap, 6.0mm; scan time, 150ms/frame. All subjects were instructed to breath normally during the acquisition process. The image acquisition experiment was conducted under the approval of the Ethical Review Board of Chiba University. The software used to implement our method

was MatLab 7.10 and we ran it on a PC with Intel®Core™2 Quad, 2.66GHz, 16GB RAM.

1.2.2. Coordinate system and image acquisition

In this subsection, we define a coordinate system and variables and then describe the method for image acquisition. We show specific values for some parameters to clarify the process and provide a practical situation for readers.

We first define a 3D coordinate system as shown in Figure 1.1. Two types of 2D-MR images are used: the navigator slice (NS) and the data slice (DS). The NS is a temporal sequence of 2D-MR images in the sagittal plane which consists of several hundred frames. Those MR images are obtained at a constant X axis position and consist of several respiratory patterns in all acquisition data. We formally denote signal intensity of a frame in NS as $f_{navi}(X_s, y, z, t_{navi})$ where t_{navi} represents the t_{navi}-th frame in NS. Here, X_s represents the X axis position where the NS is located and (y, z) represents the position in the NS.

The DS is the temporal sequence of 2D-MR images in the coronal plane. One set of DS consists of DSs along the Y axis (anterior-posterior) to cover the thoracic volume. Each of the DSs in the DS set also consists of several hundred frames and has some respiratory patterns in all breathing phases. The signal intensity in the DS is denoted as $f_{data}(x, y_i, z, t_{data})$, $i \in 1, 2, 3, \ldots, n$. Here y_i represents the Y axis position where the ith DS is located, (x, z) represents the pixel position in the DS, and n represents the number of DSs.

When the NS and DS are at the same respiratory phase, they should share the same signal intensity at (X_s, y_i) along the Z axis and ideally the following expression should be satisfied:

$$f_{navi}(X_s, y_i, z, t_{navi}) = f_{data}(X_s, y_i, z, t_{data}) \quad (1.1)$$

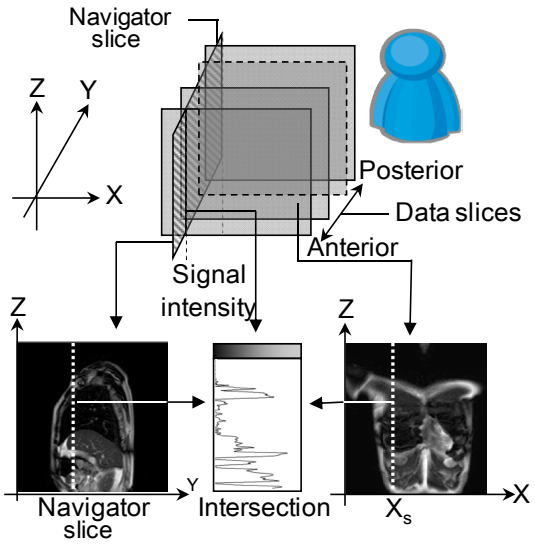

Figure 1. 1. Coordinate system of the proposed method. Navigator slice intersects with data slices at the location (X_s, y_i*)*

Although the NS and DS intersect at the location (X_s, y_i), they are not obtained at the same time. The NS is obtained first at X_s and sequentially followed by DS acquisition at the location y_i, i=1, 2, 3, …, n. The total time of image acquisition for one subject is equal to 3 min for NS acquisition and n min to obtain n slices for the DS. Normally, about 10-25 slices are obtained for the DS set. Thus, the total acquisition time to get a complete data set ranges from 13 to 28 min.

1.2.3. Description of intersection profile method

Figure 1.2 shows a schematic illustration of the intersection profile method. Because the DS and NS intersect at y_i, i=1, 2, 3, …, n, n spatio-temporal (ST) patterns can be generated from both the NS and DS at the intersection location. These ST patterns represent breathing cycles at a location (X_s, y_i) over time. Several respiratory patterns

can be extracted from ST patterns generated from the NS. The idea of the intersection profile method is to employ the similarity of respiratory patterns found in ST patterns from the NS and ST patterns from the DS. The respiratory patterns found in the NS are used as references and compared with the ST patterns from the DS. A similarity measure using the normalized cross correlation (NCC) is used to find the best matching respiratory pattern between the reference and ST patterns from the DS. A 4D-MR image can be reconstructed once the best matching respiratory patterns are found for each intersection location (y_i). The detailed procedure to reconstruct 4D-MR images using the intersection profile method is as follows:

1. Determine the intersection location of NS and each DS, denoted as y_i where i=1, 2, 3, …n and n is the number of slices of DSs.
2. Manually set region of interest (ROI) around the diaphragm boundary of the NS.
3. Generate n ST patterns from the ROI of the NS.
4. Extract respiratory patterns from the NS. One respiratory pattern is denoted as $A_{k,i}(z, t)$, k=1, 2, … m where k denotes the kth respiratory pattern and m is the number of respiratory patterns extracted from the ST pattern. The period of the kth respiratory pattern is denoted by w_k.
5. Set ROI around the diaphragm boundary of the DSs and generate n ST patterns from each DS. Denote the ST patterns from DS as $B_i(z, t_{data})$.
6. For each $A_{k,i}$, k=1, 2, 3, …m and i=1, 2, 3, …n, find the best NCC value between $A_{k,i}$ and B_i. The best NCC value from the kth pattern at y_i is denoted as $C_{k,i}$. The time at the DS where C takes the maximum value at y_i is denoted as $t_{kbest,i.}$
7. Choose the best respiratory cycle from the NS by the selecting the highest geometric mean (geomean) using the following expression:

$$k_{best} = \arg\max\left(\Pi_{i=1}^{n}\left(C_{k,i}\right)\right)^{1/n} \qquad (1.2)$$

This best geomean value will ensure that the corresponding respiratory patterns found in the DSs have the closest similarity with the respiratory patterns found in the NS. As a result, the respiratory cycle in the reconstructed 4D-MR image is also very close to the respiratory cycle in the NS.

8. Finally, the 4D-MRI can be reconstructed by combining the DS $f_{data}(x, y_i, z, t_{data})$ where t_{data} ranges from $t_{kbest,i}$ to $t_{kbest,i}+w_{kbest,i}$.

An intuitive explanation why geomean is used in Eq. (1.2) instead of using the arithmetic mean is as follows. The geomean calculates the product of the given NCC values and then takes the *n*th root. The product of the NCC values should provide a more robust representation of the similarity measure compared to the arithmetic mean which uses the sum. For example, if an arithmetic mean is used, the NCC values of 0.9 and 0.1 will produce the same arithmetic mean as NCC values of 0.5 and 0.5, as well as NCC values of 0.7 and 0.3. The arithmetic mean (similarity measure) of those examples is 0.5, which is bias and not representing the quality of reconstructed 4D-MRI. The use of geomean will avoid such bias. From the examples above, the geomean are 0.3, 0.5 and 0.46 for the first, second and third case, respectively. The NCC value of 0.9 and 0.1 yields the lowest geomean (similarity measure) compared to the other two because one of the NCC values is very low (0.1). Therefore, using geomean to reconstruct 4D-MRI will eliminate low NCC value to be included in the reconstructed 4D-MRI. It also ensures the quality of reconstructed 4D-MRI consists of similar quality of DSs.

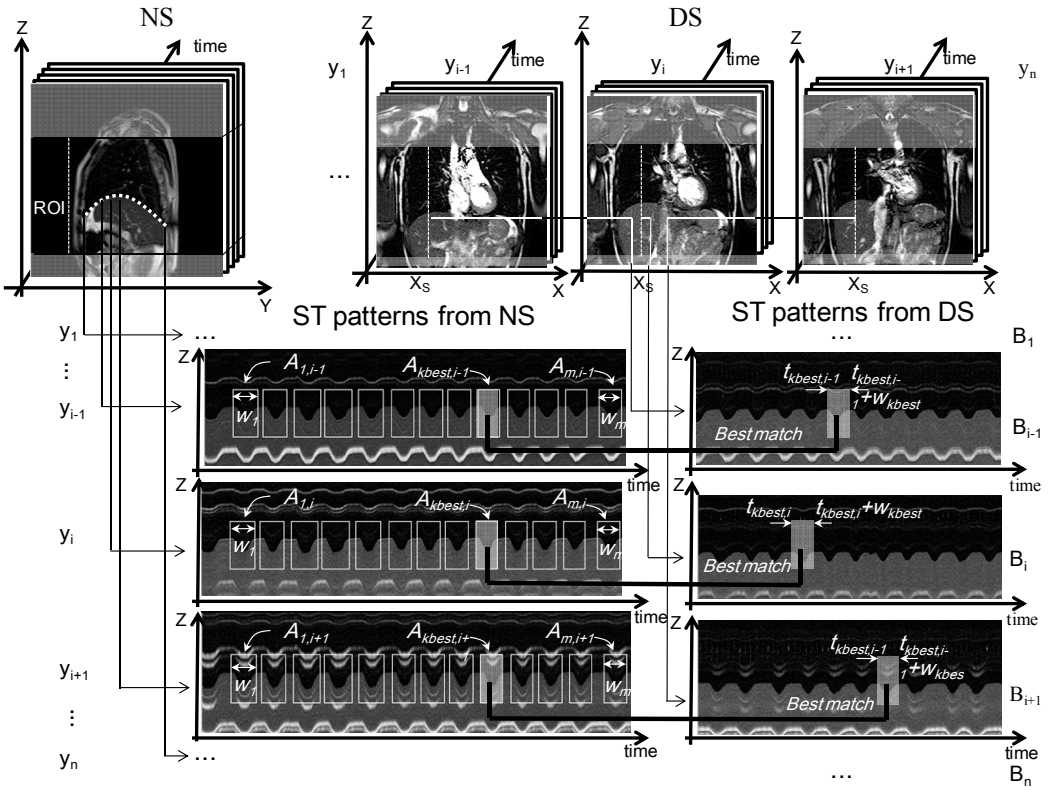

Figure 1. 2. Procedure to find a respiratory pattern from DS which is similar to that of the NS.

1.3. Thesis Contribution

The contribution of this study is mainly the improvement of the previous 4D-MRI reconstruction and clinical application of 4D-MRI. Specifically, the contributions of this thesis are:

1. Diaphragm motion extraction and modeling using GND-PCA

   Extract diaphragm motion from 4D-MRI and model using GND-PCA. We also compared the motion modeling modeled with GND-PCA and regular PCA. The error of the model using GND-PCA is smaller compared to the regular PCA.

2. Automation of 4D-MRI reconstruction.

   The automation are especially for diaphragm motion tracking and respiratory patterns extraction. Such automation is required since manual process will affect

the output of the 4D-MRI. Using automation, the reconstructed 4D-MRI will have consistent quality.

3. Time reduction of 4D-MRI data acquisition.

   In order to reduce the time acquisition, we employed a prospective method during the data acquisition. The aim is not only reduce the time acquisition but also maintaining the quality of reconstructed 4D-MRI.

4. Diaphragm motion analysis of COPD extracted from 4D-MRI

   One of the clinical application of 4D-MRI is extracting and analyzing the diaphragm motion of the COPD. We compared and analyzed the motion of the diaphragm extracted from the COPD patients and compared with healthy volunteers.

1.4. Thesis Outline

This thesis is divided into 4 major parts, statistical modeling, automatic extraction of diaphragm motion and respiratory cycle, time reduction of 4D-MRI reconstruction and clinical application of 4D-MRI. In the following chapters, we will discuss more detail on each topic.

Chapter 2 describes statistical modeling of diaphragm motion extracted from 4D-MRI using GND-PCA. The effectiveness of GND-PCA compared with general PCA to model diaphragm motion is covered in this chapter.

To support the prospective method to reconstruct 4D-MRI, chapter 3 discusses about an automatic technique to extract diaphragm motion. The automation include diaphragm motion tracking and extraction of the respiratory cycles.

Chapter 4 presents the reconstruction of 4D-MRI using prospective method. One of the advantages of prospective method is to shorten acquisition time of the data slice while maintaining the quality of 4D-MRI.

The clinical application of 4D-MRI is discussed in chapter 5. The diaphragm motion is extracted from 4D-MRI of volunteers and COPD patients. The diaphragm motion is quantitatively analyzed and also used to locate paradoxical motion of the COPD patients.

Finally, the summary and future works are presented in chapter 6.

2

GND-PCA BASED STATISTICAL MODELING OF DIAPHRAGM MOTION

Major parts of this chapter were published as a manuscript in the Journal of Computational and Mathematical Methods in Medicine:

> Windra Swastika, Yoshitada Masuda, Rui Xu, Shoji Kido, Yen-Wei Chen, and Hideaki Haneishi, "*GND-PCA-Based Statistical Modeling of Diaphragm Motion Extracted from 4D MRI*," Computational and Mathematical Methods in Medicine, vol. 2013, Article ID 482941, 9 pages, 2013. doi:10.1155/2013/482941.[*)]

[*)] Article was publish under a "Creative Commons Attribution License".

Abstract

We analyzed a statistical model of diaphragm motion using regular principal component analysis (PCA) and Generalized N-dimensional PCA (GND-PCA). First, we generate 4D-MRI of respiratory motion from 2D MRI using an intersection profile method. We then extract semi-automatically the diaphragm boundary from the 4D-MRI to get subject-specific diaphragm motion. In order to build a general statistical model of diaphragm motion, we normalize the diaphragm motion in time and spatial domain and evaluate the diaphragm motion model of 10 healthy subjects by applying regular PCA and GND-PCA. We also validate the results using the leave-one-out method. The results show that the first three principal components of regular PCA contain more than 98% of the total variation of diaphragm motion. However, validation using

leave-one-out method gives up to 5.0mm mean of error for right diaphragm motion and 3.8mm mean of error for left diaphragm motion. Model analysis using GND-PCA provides about 1mm margin of error and is able to reconstruct the diaphragm model by fewer samples.

Keywords

Statistical modeling, GND-PCA, diaphragm motion, 4D-MRI

2.1. Background

4D-MRI is an advanced imaging technique that reconstructs a 3D MRI with time series from a set of time sequential images of 2D MRI into. For respiratory motion, the use of 4D MRI has an important role in many clinical applications such as lung cancer radiotherapy planning, examining pulmonary diseases and analyzing diaphragm motion. However, current MRI is unable to acquire 4D MRI directly. Therefore, in the recent years some methods have been proposed to reconstruct 4D MRI of respiratory organs based on the sequential 2D MRI [8] [9] [13]

M von Siebenthal [8] proposed a method to obtain 4D image using internal respiratory gating and reconstructed it by retrospective sorting of dynamic 2D MR images. It showed the detailed deformation of an organ during free breathing. Tokuda also proposed an adaptive imaging method to acquire a series of 3D MR images of respiratory organs as the extension of respiratory gating [9]. Our previous study successfully achieved 4D-MR imaging of organs with respiratory motion using a method called intersection profile method [13]. In this method, we reconstructed 4D MRI of respiratory organ from time sequential images of 2D MRI under natural respiration. We not only successfully visualized 4D MRI of respiratory organ, but also proposed to construct diaphragmatic function map that can be used to evaluate diaphragm motion quantitatively. Previous related works on 4D respiratory motion modeling include [14] [15] [16] [17] [18].

Recent statistical model of respiratory motion was proposed by Li et al [19]. It was a statistical model of lung based on principal component analysis (PCA) and applied to

clinical data. The lung motion model, however, was based on two types of respiratory phantoms and cosine function which will only be idealistic for phantom motion. Extraction and statistical modeling of lung motion field was also demonstrated in [20]. The experiment extracted motion fields from a 4D-CT data set and built a motion model for both intra- and intersubject. Although it focused on the lung motion, the results showed that the use of diaphragm as a stimulator to drive the motion model could reduce the prediction error. Simultaneous registration of all dynamic MR images and modeling processing were performed in [21] for the purposes to improve the accuracy of motion estimation. However, this approach may only be feasible for simple rigid or affine motion model. Applying this model to organs that have complex or non-rigid motion will significantly increase the number of parameter and consequently execution time also becomes much larger.

The statistical modeling in was focusing on how to model respiratory motion based on lung motion [19] [20] [21] or internal liver motion [22]. In this paper, instead of extracting lung to obtain respiratory motion, we focus on extracting diaphragm motion from 4D-MRI and analyzing it using PCA. As one of the major determinant in respiratory motion, diaphragm has greater superior-interior translation compared with other respiratory organs such as lung or liver. Thus by modeling and analyzing diaphragm motion, the variability of respiratory motion can be clearly visualized. As mentioned in [23], GND-PCA method can construct MR T1-weighted brain volumes and CT lung volumes using fewer training samples compared with regular PCA. Hence, we also interested to analyze the efficacy of GND-PCA compared with regular PCA in modeling the diaphragm motion.

To the best of our knowledge, this is the first study of modeling and analyzing diaphragm motion extracted from 4D MRI.

2.2. Materials and Methods

The process of constructing and analyzing the diaphragm motion model consists of four parts. The first is diaphragm segmentation and motion tracking. We will briefly review the methodology we used to create 3D model of diaphragm shape. Second is data normalization. We will cover how to normalize the data obtained from the previous step. This step is primarily important to generalize the data from different subjects. Third is model analysis using PCA and GND-PCA. Basic theory of PCA and GND-PCA will be described. Last is data evaluation which we will explain how to validate the constructed model.

2.2.1. 3D Diaphragm Segmentation and Motion Tracking

Right-handed Cartesian coordinate system is used to cover the whole diaphragm area. A number of MRI data slices, size of 256x256 pixels in coronal view are set along the y axis (Fig. 1a). Each data slice position is denoted as y_i where i=1,…, S. To assess the diaphragm motion, we also use T time-sequential images for each data slice of y_i. We denote one data slice as $f_{data}(x, y_i, z, t)$, where t=1, 2, …, T. A first shape of diaphragm is obtained from $f_{data}(x, y_i, z, t)$ for i=1, 2, …, S and t=1. The diaphragm shape is determined as follows. Several points are selected in each data slice (y_i) that represents diaphragm boundary shown as white dots in Fig. 1a. The number of points varies from 10 to 15 depend on the curve of diaphragm boundary. Generally, more points are required if the diaphragm boundary has a rounded or curvature shape. The points are then connected by spline interpolation. By conducting this operation for all yi,

the area of diaphragm in xy plane is defined as shown in Figure 2.1. We denote this shape as Ω. Note that we ignore the area below the heart because it is strongly affected by heart beat and apart from respiratory motion. The entry of this matrix represents z value of diaphragm surface at (x,y). The 3D representation of diaphragm surface is shown in Fig. 1c. In this step, S x 256 matrix for one whole diaphragm area is generated, where S is the number of slice. Depends on the acquisition process, S will vary between 16 to 24.

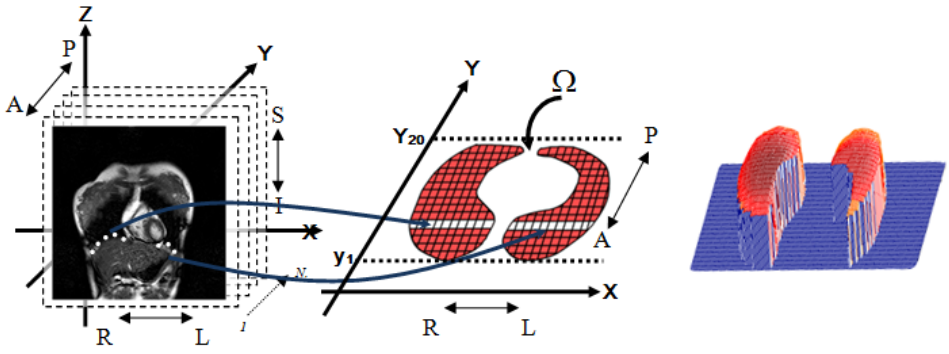

(a) (b) (c)

Figure 2. 1. Coordinate definition of 4DMRI and diaphragm extraction. (a) Manually selecting several points (white dots) of one data slice to extract diaphragm surface, (b) complete extraction of diaphragm surface from y1 to y20 and (c) representation of diaphragm area.

Once the 3D shape on diaphragm area Ω is obtained for t=1 (as shown in Figure 2.1b), the 3D shape of diaphragm over the area of Ω is tracked in the next frame. In order to do so, a profile of $f_{\text{data}}(x, y_i, z, t)$ along Z at position (x, y) over Ω is compared with a profile of $f_{data}(x, y_i, z, t\text{-}1)$ at the same position (x, y_i) and find a value of displacement of diaphragm along z axis by using normalized cross correlation.

Figure 2.1 summarizes the flow diagram of diaphragm motion tracking method. Complete reference regarding this motion tracking method can be found in [13].

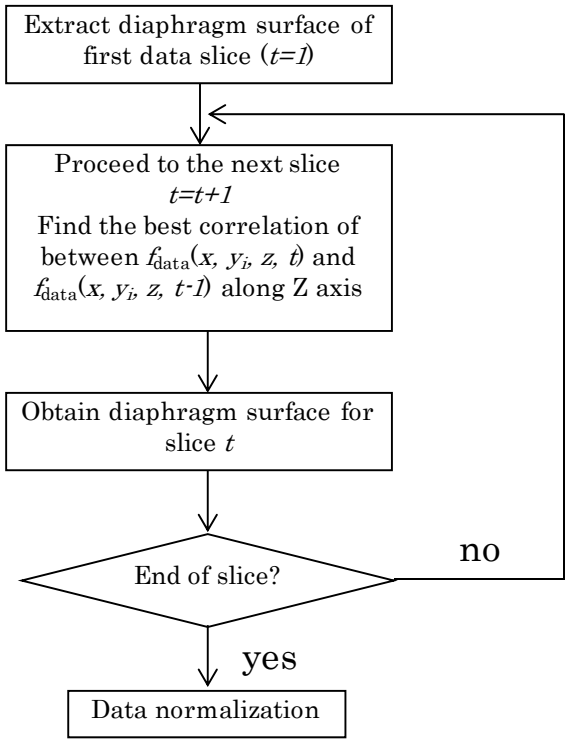

Figure 2. 2. Flow diagram of diaphragm motion tracking method.

2.2.2. Data Normalization

The acquisition of diaphragm motion based on the previously explained method cannot be generalized for all diaphragms due to the wide range of variability of diaphragm shape and size among the subjects. Hence, the acquired data need to be normalized. The normalization process takes four steps.

First, we divide the diaphragm area into two parts, right and left diaphragm area.

Second, to represent a detailed and unique diaphragm region, we calculate gradient edges of all diaphragm shapes and choose one that has the highest gradient edges as reference image. Affine registration is then performed for all diaphragm shapes to ensure the same location and size of all diaphragm shape before the analysis is performed.

Third, for each diaphragm area, we set the top left and bottom right coordinate to limit the diaphragm area into a rectangular shape. The distance of new top left position is 1/10 of the diaphragm area width and so is the new bottom right position. Figure 2.3 shows how to set new region of diaphragm area. Selecting the region of diaphragm area ensures that the analysis is only done in the main part of the diaphragm area and ignores the area that has small movement. This also maintains the correspondence on different subjects since the top and bottom area will constantly represent same anterior and posterior position of all subjects.

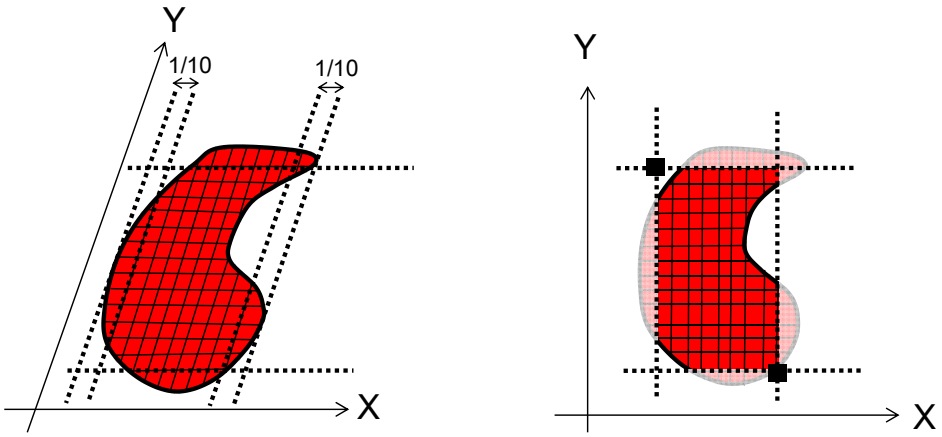

Figure 2. 3. Set the top left and bottom right coordinate to limit the diaphragm area

The last step of normalization process consists of two parts, temporal and spatial normalization. Temporal normalization makes all subjects have the same number of frames, while spatial normalization only normalizes the size of diaphragm area.

Let Z(x,y,t) denotes the z value of diaphragm surface (or target image) at (x,y) position and t^{th} frame (1, 2, …, T). After temporal normalization Z(x, y, t) can be denoted as Z(x, y, t*) where t* range from 1 to 20. The following operator is used to define t*:

$$t^* = \left\lfloor \frac{20-1}{T-1}(t-1) + 1 \right\rfloor \qquad (2.1)$$

Here the operator ⌊ ⌋ represents ceiling function which returns a decimal number to its smallest integer.

Due to fact that the coordinate position and the size of rectangular area shown in Figure 2.3 vary among the subjects, the last part in the normalization process is to fix the rectangular area for both y and x axis. The purpose is that all the data will have the same size and position. The size of the reference image is represented by $W_{ref} \cdot H_{ref}$. In our study, we used 60x100 pixels for $W_{ref} \cdot H_{ref}$. Actual normalization process is described as follows.

1. *Normalization of Y axis*. To normalize the diaphragm area into Y axis, the origin image is scaled and fixed to the reference image. The following operator is used to scale diaphragm area in Y axis.

   $$Z'(x, y, t) = Z(x, \left\lceil \frac{H_{target}}{H_{ref}} y \right\rceil, t^*) \qquad (2.2)$$

   where H_{target} is height of the image target and H_{ref} is the height of the reference image. Operator ⌈x⌉ represents ceiling function which rounds up the decimals into an integer. This scaling process is done for all x and y. The results of Y axis normalization is called intermediate image.

2. *Normalization of X axis*. The width of the reference image is also fixed by horizontal scaling. The operator used to scale diaphragm area in X axis is written as:

   $$Z''(x, y, t) = Z'(\left\lceil \frac{W_{target}(n) - W_{target}(1)}{W_{ref}} x + W_{target}(1) \right\rceil, y, t^*) \qquad (2.3)$$

   where $W_{target}(n)$ and $W_{target}(1)$ are the last and first non-zero position in the current y axis and W_{ref} is the width of the reference image. This horizontal scaling is done for all x, y. The result of X axis normalization is a final image with the same width and height from the reference image.

Since there are both right and left diaphragm area, scaling the area using the reference image is done for both diaphragm areas. This process is repeated for each data frame obtained from the previous algorithm starting from the first time-sequential image to the last one (t*=1..20).

The matrix dimension of diaphragm motion after normalization is W_{ref} x H_{ref} x 20 or equals to 60x100x20 (spatial size of reference image x 20 frames) for each side of diaphragm. To ensure the diaphragm motion is represented as a whole diaphragm and keeping the shape variance, we merge right and left side of diaphragm into a matrix. The final matrix dimension after the merging is 60x200x20. Considering the data as high dimensional data, linear statistical analysis is possible to be carried out by applying principal component analysis (PCA). It reduces the data set and reveals the hidden pattern as maintaining majority of the variation in the original data.

Upper part of Figure 2.4 shows the spatial normalization process of certain frame. After modeled using PCA, we reverse the image into original diaphragm shape. Firstly, we create a mask based on the original diaphragm shape. Using this mask the modeled image is then resized and reshaped to the original diaphragm shape. The bottom part of Figure 2.4 shows the reversing process from a frame modeled by PCA to a diaphragm shape image.

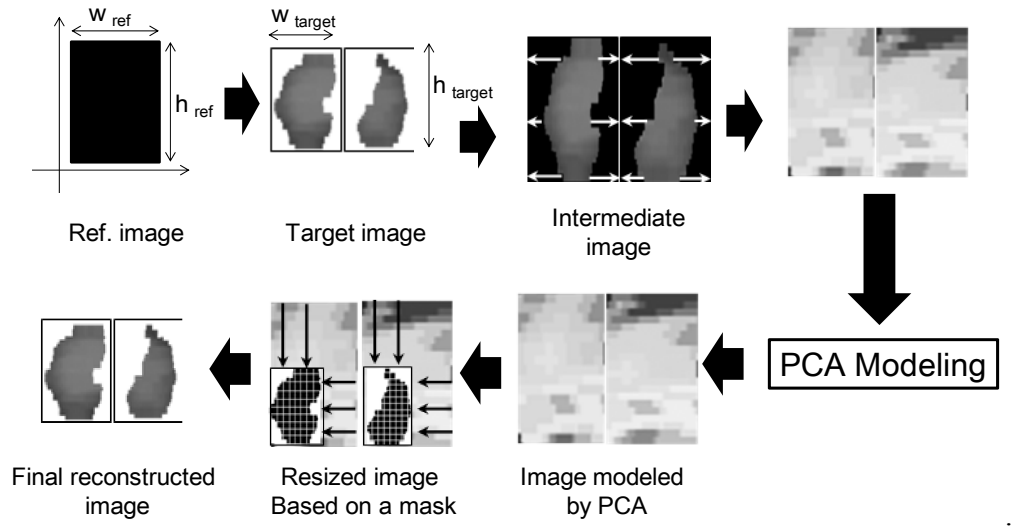

Figure 2. 4. Diagram of spatial normalization and its reconstruction process to obtain diaphragm original shape.

2.2.3. PCA and GND-PCA diaphragm motion model

Generally, PCA is a statistical method to transform a set of correlated variables into a smaller number of uncorrelated variables or principal components (PCs). The PCs are sorted in the descending order of importance. The purpose of PCA is that the first few PCs are able to explain large proportion of the variation in the original variables, and only those PCs are retained for further analysis.

The following paragraphs describe how PCA is used to analyze diaphragm motion. Let $\mathbf{z}$ be a vector of z value of the spatio-temporally normalized for both right and left diaphragm. Vector $\mathbf{z}$ can be expressed as 1D array:

$$\mathbf{z} = [z_1, z_2, z_3, \ldots z_N]^T \quad (2.4)$$

where

$$z_i = Z(x, y, t) \quad (2.5)$$

and i is the index obtained by the following equation:

$$i = (t-1)H_{ref}W_{ref} + (y-1)H_{ref} + x \quad (2.6)$$

For *m* subjects, we denote $\mathbf{z}^{(j)}$ (j=1, 2, 3, …, m) as a diaphragm motion data set from j-th subject.

Principal components are the eigenvectors with its corresponding eigenvalues of covariance matrix of **z**. The sorted eigenvectors by decreasing order of its corresponding eigenvalues is the most optimal with respect to information loss.

Another method to build a statistical method is GND-PCA. It is a method to model a series of multi-dimensional array proposed by Xu [23]. Instead of using one long vector to represent a motion model, GND-PCA uses a tensor to represent a shape or motion model. The tensor itself is a multi-dimensional array whose order is the number of dimensions, also known as ways or modes. We will give a brief explanation of GND-PCA. More details about GND-PCA can be read in [23].

An Nth-order tensor, denoted by $\mathcal{A}$, where $\mathcal{A} \in \mathbb{R}^{I1 \times I2 \times I3 \times \ldots \times In}$ and $\mathbb{R}^n$ denotes the set of all vectors with *n* real components. In tensor point of view, a vector and a matrix are a tensor of order one and order two, respectively. One diaphragm motion can be considered as third-order tensor $\mathcal{M}$, where $\mathcal{M} \in \mathbb{R}^{I1 \times I2 \times I3}$ ($I_1 \times I_2$ is the spatial dimension of the diaphragm in each frame and I_3 is the number of frame).

Here let $\mathcal{M}_i$ (i=1, 2, 3, …, *m*) denotes *m* samples of third-order tensor that represents diaphragm motion from *m* subjects. A series of lower rank tensors $\mathcal{M}_i^* \in \mathbb{R}^{J1 \times J2 \times J3}$ is defined as the most accurate approximation of original tensors $\mathcal{M}_i$ where $J_1 < I_1$, $J_2 < I_2$ and $J_3 < I_3$. To obtain $\mathcal{M}_i^*$, we decompose the tensors into smaller core tensors and its corresponding orthogonal mode matrices shown by:

$$\mathcal{M}_i^* = \mathcal{C}_i \times_1 \mathbf{Y} \times_2 \mathbf{X} \times_3 \mathbf{T} \qquad (2.7)$$

The product $_n\mathbf{X}$ denote the n-mode product between the tensor and the mode matrices [23]. Figure 2.5 shows the illustration of 3rd order tensor decomposition of diaphragm motion model.

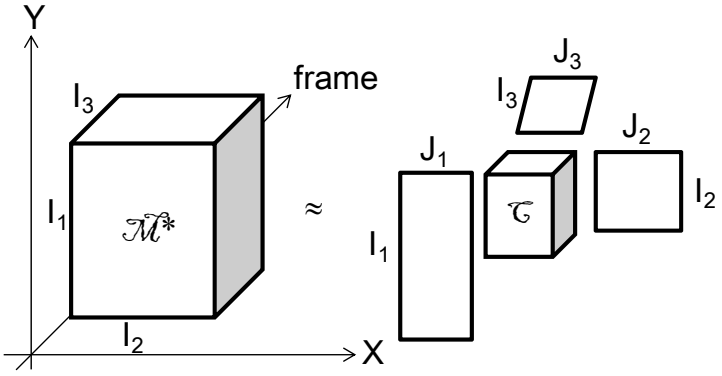

Figure 2. 5. Decomposition of 3rd order tensor into one core tensor and three mode matrices.

The orthogonal mode matrices capture the variation along the spatial ($\mathbf{Y}\in\mathbb{R}^{I1xJ1}$ and $\mathbf{X}\in\mathbb{R}^{I2xJ2}$) and time ($\mathbf{T}\in\mathbb{R}^{I3xJ3}$) dimension. The core tensors ($\mathcal{G}_i\in\mathbb{R}^{J1\ x\ J2\ x\ J3}$) control the interaction between mode matrices and can be seen as the compressed version of the original tensor. The mode matrices can be obtained by solving the following equation:

$$\min \| \mathcal{M}_i - \mathcal{M}_i^* \| = \min \| \mathcal{M}_i - \mathcal{G}_i \times_1 \mathbf{Y} \times_2 \mathbf{X} \times_3 \mathbf{T} \| \qquad (2.8)$$

2.2.4. Evaluation Methods

In this study, we evaluate the performance of the diaphragm motion model by calculating mean and maximum errors of the constructed model. Leave-one-out method is used for this evaluation [24].

The error of approximated model from each subject can be obtained by simply subtracting each of the elements of constructed model from the original shape and getting the absolute value. The error of right and left diaphragm shape of *j*-th subject can be mathematically written as:

$$e^{(j)}(x,y,t) = \left|\hat{z}^j(x,y,t) - z^{(j)}(x,y,t)\right| \quad (2.9)$$

Here we redefined the shape of normalized diaphragm by $z^{(j)}(x,y,t)$.We also represent the estimate by the statistical model by $\hat{z}^{(j)}(x,y,t)$.

Based on this definition of error, some kinds of mean or maximum error can be expressed. For instance, mean error of each subject is given by:

$$e_{mean}{}^{(j)} = \frac{1}{\mathrm{n(j)T}}\sum_{\mathrm{t=1}}^{\mathrm{T}}\sum_{\mathrm{x,y}\in\Omega^{(\mathrm{j})}} e_k^{(j)}(x,y,t) \qquad (2.10)$$

where $n^{(j)}$ is the number of non-zero values in the diaphragm area $\Omega^{(\mathrm{j})}$ of j-th subject. Inter-subject average of $e_{k,mean}{}^{(j)}$ is given by:

$$e_{mean} = \frac{1}{\mathrm{m}}\sum_{\mathrm{j=1}}^{\mathrm{m}} e_{mean}{}^{(j)} \qquad (2.11)$$

The maximum error for *j*-th subject is given by:

$$e_{max}^{(j)} = \max\left(e^{(j)}(x,y,t)\right) \qquad (2.12)$$

We can also calculate the inter-subject average of maximum error by:

$$e_{max} = \frac{1}{m}\sum_{j=1}^{m} e_{max}^{(j)} \qquad (2.13)$$

Another evaluation method we used is frame-by-frame error calculation. Frame-by-frame error is important to analyze which respiratory phase gives the largest or smallest error. Frame-by-frame mean error of each subject is given by:

$$e^{(j)}(t) = \frac{1}{n^{(j)}}\sum_{x,y} e^{(j)}(x,y,t) \qquad (2.14)$$

Inter-subject average of frame-by-frame error is given by:

$$e(t) = \frac{1}{m}\sum_{j=1}^{m} e^{(j)}(t) \qquad (2.15)$$

2.3. Experimental Results

Ten healthy subjects within the age ranging from 23 to 46 participated in this study. For diaphragm motion studies, MR Images are particularly preferred than CT images since MR images provide high soft tissue contrast to produce detailed respiratory organs. The high contrast of MR images will be useful during the manual diaphragm boundary segmentation process.

In this study, MR Images were acquired using 1.5T INTERA ACHIVA nova-dual (Philips Medical Systems) whole-body scanner with a 16ch SENSE TORSO XL Coil. A 2D balanced FFE sequence was used. The imaging parameters are as follow. SENSE factor: 2.2, flip angle: 45^{o}, TR: 2.2ms, TE: 0.9ms, FOV: 384mm, in-plane resolution 256x256 pixels and $1.5x1.5mm^2$, slice thickness: 7.5mm, slice gap=6.0mm, scan time: 150ms/frame and 400 frame/slice. Normal breathing was instructed for all subjects during the acquisition process. This image acquisition experiment was conducted under an approval of Ethical Review Board of Chiba University.

The software used for PCA is MatLab 7.10 and running on PC with Intel®Core™2 Quad, 2.66GHz, 16GB RAM.

2.3.1 PCA and GND-PCA Model Output

The contribution ratio and cumulative up to three principal components of right and left diaphragm motion are listed in Table 2.1. The percentage of variance of first principal component is 97.4% and 99.2% for the first three principal components.

Table 2. 1. Percent variations and cumulative contribution up to three principal components of 10 healthy subjects

PC	%	Cum. %
1	97.4	97.4
2	1.1	98.5
3	0.7	99.2

Mapping the error of z coordinates in the constructed model using different number of PCs will be useful for further analysis. Figure 2.6 and Figure 2.7 illustrate color mapping of the error in the first frame of the first subject given by:

$$e^{(1)}(x, y, 1) = \hat{z}^{(1)}(x, y, 1) - z^{(1)}(x, y, 1) \qquad (2.16)$$

Note that the error is not absolute value as expressed in Eq. (2.9).

The white area represents the exact approximation, red and blue are indicate that estimated z coordinates is higher and lower than the actual position, respectively.

Figure 2.6 is the case when first one, first two and first three PCs are used in regular PCA respectively. As shown in Figure 2.6c, the red and blue areas are decreasing. This indicates that the model well approximated the actual shape when the first three PCs were used.

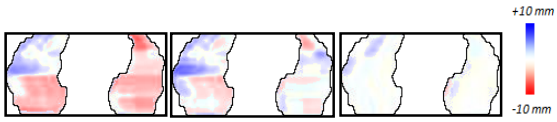

(a) (b) (c)

Figure 2. 6. Regular PCA Error position mapping of one frame using (a) First PC (b) First two PCs and (c) First three PCs.

The similar results are also shown by GND-PCA construction as illustrated in Figure 2.7. The error color mappings were obtained by reconstructing the model with 4x2x1, 8x4x2, 16x8x4, 32x16x8 and 64x32x16 core tensors respectively and subtracting them from the original shape of diaphragm. The last three core tensors

showed that the red and blue colors on the diaphragm area are almost disappeared which means the constructed models are very similar to the original shape.

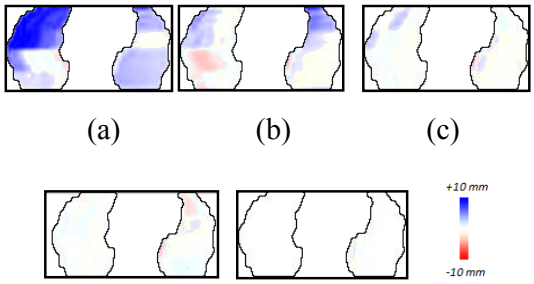

Figure 2. 7. GND-PCA error position mapping of one frame using (a) 4x2x1 (b) 8x4x2 (c) 16x8x4 (d) 32x16x8 and (e)64x32x16 core tensors.

In term of number of coefficients required to construct the model, regular PCA outperformed the GND-PCA. Table 2. 2 shows the comparison of the number of coefficients required to construct diaphragm motion model between regular PCA and GND-PCA.

Table 2. 2. Comparison the number of coefficients required to construct diaphragm motion model

Regular PCA		GND-PCA	
PC	Coef.	Core tensor	Coef.
First PC	1	4x2x1	8
First two PCs	2	8x4x2	64
First three PCs	3	16x8x4	512

2.3.2. Leave-one-out Method Validation

We omitted one subject as a testing subject and constructed the diaphragm motion model using training data from the remaining nine subjects. This model was then

applied to the testing subject. The mean error of the testing subject was calculated using Eq. 2.10. The whole procedure is repeated till each of ten subjects has become testing subject once.

Figure 2.8a shows the mean error of each subject in case of model using regular PCA and GND-PCA, respectively. For regular PCA model, the mean error ranges are 3.8-13.4mm for first PC, 3.6-10.2mm for first two PCs and 3.5-10.6mm. Although more than 98% variability of the diaphragm motion can be covered by the first three PCs as shown in Table 2.1, the validation using leave-one-out method showed that inter-subject the average of mean error of the model given by Eq. 2.11 is more than 4 mm.

Contrary to the regular PCA, the error mean of model by GND-PCA as shown in Figure 2.8b is much smaller. The mean error ranges are 1.4-9.0mm for 4x2x1 core tensor, 1.4-4.0mm for 8x4x2 core tensor and 0.8-2.1mm for 16x8x4.

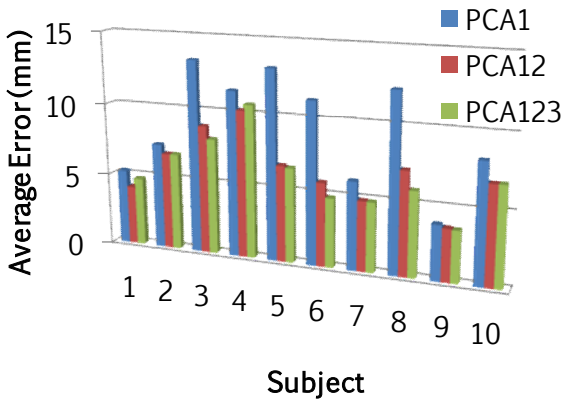

(a)

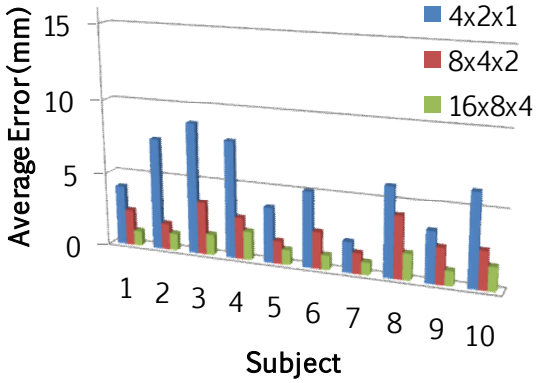

(b)

Figure 2. 8. The mean error of the model by (a) regular PCA from and (b) GND-PCA. The measurement unit is in mm.

Figure 2.9 showed frame-by-frame mean error $e(t)$ of the model by regular PCA. As shown in this figure, 18-20th frames indicate low mean error (about 3.9mm on average) and 9-11th frames indicate high mean error (about 9.0mm on average). It is probably caused by the smaller variability in the 18-20th frames and higher variability in 9-12th frames.

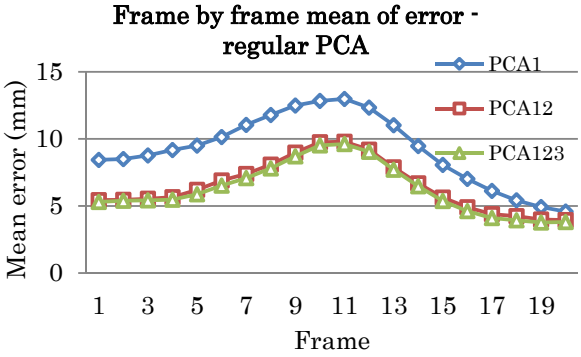

Figure 2. 9. Regular PCA mean of error frame-by-frame

Different results were obtained using GND-PCA as shown in Figure 2.10. Since GND-PCA can capture both spatial and time variability; there were no large differences of mean error among the frames. For instance, the standard deviation of mean error from 16x8x4 core tensors is 0.37mm, while for three principal components of regular PCA the mean error is 2.2mm.

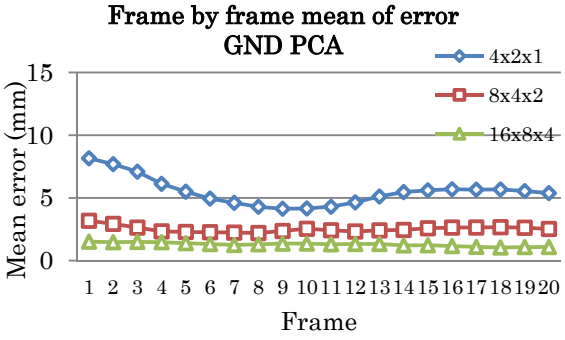

Figure 2. 10. GND-PCA mean of error frame-by-frame

Table 2.3 summarizes the average of mean error e_{mean} and average of maximum error e_{max}. The results of GND-PCA, showed consistent reconstruction with smaller error compared with the model constructed using regular PCA.

Table 2. 3. Leave-one-out method validation using regular PCA: mean and average of maximum error position (in mm)

Used PC	Regular PCA		GND-PCA	
	Mean	Max	Mean	Max
1st PC	9.2	15.7	5.5	13.5
1st+2nd PCs	6.5	17.3	2.4	8.1
1st+3rd PCs	6.3	17.2	1.3	5.5

2.4. Discussion

In this paper, we described how to build a statistical model of diaphragm motion using PCA and GND-PCA. The model was obtained from 4D-MRI that reconstructed from time sequential images of thoracic 2D MRI of ten healthy subjects. The modeling process involves manual segmentation of diaphragm boundary, automatic motion tracking based on the intersection profile method [13], constructing region of interest for right and left area of diaphragm and normalization of diaphragm shape.

The developed model using regular PCA can accurately describe more than 98% of the total variation by including the first three PCs. This indicates that most of the diaphragm motion variability are adequately described using a few number of parameters. Consequently, the description and motion of the diaphragm are greatly simplified by this model.

Leave-one-out validation was employed to evaluate the performance of the model. As shown on Table 2.3, the results of regular PCA illustrated that mean error position of both side of diaphragm was more than 6.0mm, which considered as large error.

To build a better statistical modeling, we applied GND-PCA [23]. Differs from regular PCA, GND-PCA is not necessarily unfolding the diaphragm motion model into one long vector. Instead, it decomposes the model into a core tensor and several mode matrices for dimensionality reduction. The mode matrices can represent the principal axes of variation. Several numbers of core tensors are chosen to construct the motion model. The smallest size of core tensor is 4x2x1 which is able to construct the motion model under leave-one-out validation with mean error of 5.5mm. Among the three sizes of core tensor (4x2x1, 8x4x2, and 16x8x4), the best model construction is achieved by 16x8x4 core tensor which gives mean error of 1.3mm. The maximum error is also significantly reduced to 5.6mm. Compared with regular PCA using first three PCs, the results of GND-PCA showed significant improvement to the motion model. Mean error obtained from frame-by-frame analysis as shown in Figure 2.10 also confirmed that GND-PCA is able to capture the motion variability of the diaphragm. One of the major drawbacks of GND-PCA is that it requires more coefficients to construct the model compared with regular PCA.

There are some considerations regarding the diaphragm motion model in this study. The first is the resolution of MR images used in this study limits the motion model for being used in the clinical application such as radiotherapy planning. At this stage, our main focus is to demonstrate that GND-PCA can model the diaphragm motion with smaller number of sample data compared with regular PCA. The model cannot be applied for the clinical application due to the low MR image resolution. Higher resolution of MR image is required if one needs to apply the model for a clinical application.

Second is about shape modeling approach. In this study, we used simple spatial and temporal normalization. Although this simple normalization is sufficient to show the efficacy of GND-PCA compared with regular PCA, the use of other spatial normalization techniques such as active point distribution model [25] or non-rigid registration [26] such as thin-plate splines or cubic B-splines will provide a better diaphragm motion modeling. We will consider this issue in our future works.

Other consideration is that the manual segmentation of diaphragm area can affect the final results. Manual segmentation of diaphragm boundary is very subjective to the experience of the user. Hence, the variability of the diaphragm motion may change when the diaphragm area is resegmented. An automatic statistical shape model of diaphragm area from thoracic 2D MRI is needed to be developed for further work. Although proposed method in [27] can be used to develop a statistical shape model of diaphragm, it suits only for respiratory-gated CT data-sets. Several adjustments need to be done to apply the method to thoracic 2D MRI.

2.5. Conclusion

We have developed a statistical method to model diaphragm motion using PCA. Time-sequential 2D MRI were constructed from a 4D MRI and extracted to obtain a 3D diaphragm motion model. Regular PCA and GND-PCA were then applied to construct model. In the experiment, we investigated that three eigenvectors or PCs with the largest eigenvalues are sufficient to accurately describe diaphragm motion model from ten healthy subjects. Model validation using leave-one-out showed that GND-PCA gives more stable reconstruction compared with regular PCA. This concludes that GND-PCA can model the motion better with a small numbers of sample data. Further

works to be done include automatic segmentation of diaphragm area and investigation of compactness, generality, and specificity of the model.

Acknowledgments

This work was supported in part by Grant-in-Aid for Scientific Research on Innovative Areas (No. 22103504 and No. 24103703), Computational Anatomy, from the MEXT, Japan.

3

AUTOMATIC EXTRACTION OF DIAPHRAGM MOTION AND RESPIRATORY PATTERN

Major parts of this chapter were published as a manuscript in the Journal of TELKOMNIKA:

Windra Swastika, Yoshitada Masuda Takashi Ohnishi and Hideaki Haneishi: "*Automatic Extraction of Diaphragm Motion and Respiratory Pattern from Time-sequential Thoracic MRI*", TELKOMNIKA, Vol.14, No.2, pp. 329-334 (2015) *)

*) *Used with the permission of the Journal of TELKOMNIKA*

Abstract

Thoracic time-sequential MRI can be used to assess diaphragm motion pattern without exposing radiation to subject. Clinicians may employ the motion to evaluate the severeness of chronic obstructive pulmonary disease (COPD). This study proposed a diaphragm motion extraction method on time-sequential thoracic MRI in sagittal plane. Otsu's threshold and active contour algorithm are used to obtain diaphragm boundary. An automatic diaphragm motion tracking and extraction of respiratory pattern are also performed based on the diaphragm boundary. A total of 1200 frames time-sequential MRI in sagittal plane was obtained for total of 15 subjects (8 healthy volunteers and 7 COPD patients). The proposed method successfully extracts diaphragm motion and respiratory patterns for both healthy volunteers and COPD patients.

Keywords

magnetic resonance imaging, chronic obstructive pulmonary disease, respiratory pattern, diaphragm motion.

3.1. Introduction

Diaphragm is a dome-shape respiratory organ located below the lung that separates chest from the abdomen. It controls the movement of the lungs and the breathing process (inhalation and exhalation). The motion of the diaphragm can be used to evaluate the severeness of chronic obstructive pulmonary disease (COPD) [28]. Hence, in the past few decades diaphragm motion has been assessed in several studies [28] [29] [30] [31] [32] [33]. In 1985, Diament et al. [29] extracted diaphragm motion from ultrasonography to evaluate diaphragm motion abnormalities. Gerscovich et al. [30] and Boussuges et al. [31] used M-mode ultrasonography to record diaphragm motion in two dimensions. Despite its portability, real-time examination and no ionization radiation, due to the nature of ultrasonography the imaging result does not reveal tissue density and potentially creates artifacts. The use of magnetic resonance imaging, which provides more clear and detailed images of soft tissue, has been proposed in [32] [33] [34]. However, none of them use automatic extraction to extract diaphragm motion and respiratory pattern.

In this study, we focused on automatic extraction of diaphragm motion from a time-sequential thoracic MRI in sagittal plane. The extraction results were used to calculate diaphragmatic dome factor (Kdome) and diaphragm displacement. We then compared the statistical analysis of Kdome and diaphragm displacement from COPD patients and healthy volunteers.

3.2. Subjects and methods

This section describes the image acquisition and the methods of automatic diaphragm motion extraction including respiratory pattern extraction.

3.2.1. Image acquisition

The MR images were acquired using 1.5T INTERA ACHIVA nova-dual (Philips Medical Systems) whole-body scanner with a 16ch SENSE TORSO XL Coil. A 2D balanced FFE sequence was used. The imaging parameters are as follow. SENSE factor: 2.2, flip angle: 45^{o}, TR: 2.2ms, TE: 0.9ms, FOV: 384mm, in-plane resolution 256x256 pixels and 1.5x1.5mm^2, slice thickness: 7.5mm, slice gap=6.0mm, scan time: 150ms/frame.

Normal breathing was instructed for all subjects during the acquisition process and total of 1200 frames in sagittal plane were obtained for each subject. Image acquisition experiment was conducted under an approval of Ethical Review Board of Chiba University.

3.2.2. Diaphragm motion extraction

In order to get diaphragm motion, we first define a region of interest (ROI) of the MR image by cropping the image that covers the diaphragm boundary. Typically, diaphragm boundary is located in middle of MRI in sagittal plane. To cover the whole area of diaphragm boundary, we first define two parameters, h and w to represent the width and height of ROI.

There two main steps to extract diaphragm motion. The first step is to obtain diaphragm boundary for the first frame only using active contour algorithm. Once the first frame of diaphragm boundary is obtained, the next step is to extract the diaphragm boundary for the subsequent frames based on normalized cross correlation (NCC) value. The complete processes of diaphragm motion extraction are as follows.

We first perform clustering-based image thresholding using Otsu's thresholding method [35]. After the thresholding process, the diaphragm area became clearly

distinguishable from other organs. A mask is created above the diaphragm boundary as seed point in order to trace the diaphragm boundary using active contour algorithm [36]. Note that this process is only performed for the first frame only. Figure 3.1 shows the process of obtaining diaphragm boundary of the first frame.

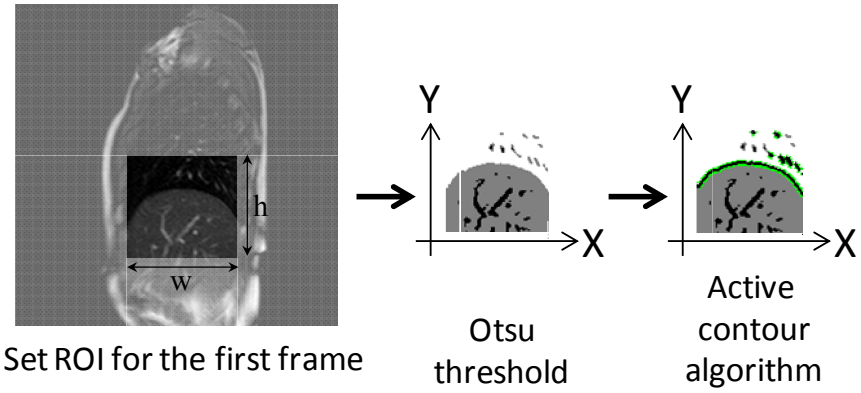

Figure 3. 1. Obtaining diaphragm boundary for the first frame.

To get diaphragm boundary for the subsequent frames, we utilize one column matrices template defined by T_x where x=1..w. The element of matrix T_x is obtained from pixel values of the ROI at column the x. Therefore, the size of matrix T_x is $1xh$, where h is the height of the ROI. It is also necessary to generate a 2D spatio temporal of column x (Figure 3.2a). The location of diaphragm boundary at column x for the subsequent frames is defined by the highest NCC value between the matrix T_x and the 2D spatio temporal of the subsequent frames at column x. The process is repeated for x=$1..w$. We denoted the position of the diaphragm boundary at location x as $f_x(i)$ where i represents the ith frame. The $f_x(i)$ shows periodic peaks and valleys associated with respiration cycles. Figure 3.2 illustrates how to determine the location of diaphragm boundary.

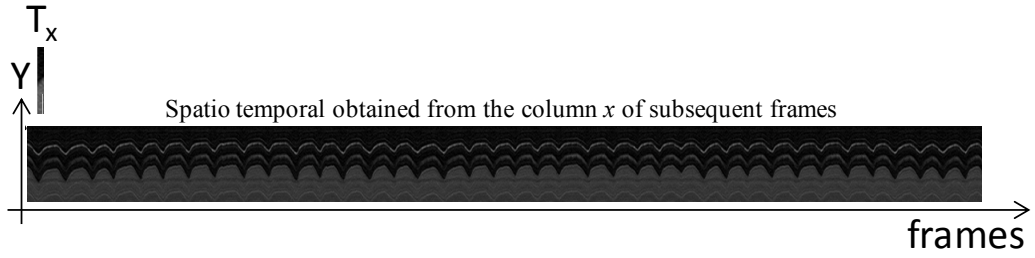

(a)

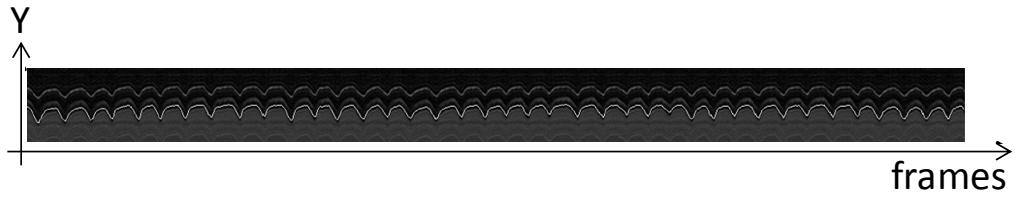

(b)

Figure 3. 2 Determine the location of diaphragm boundary. (a) Element of matrix T_x *is obtained from the pixel values of ROI at column* x *and the spatio temporal is generated at the column* x *from the subsequent frames; (b) The detected diaphragm motion at column* x *(*$f_x(i)$*), is represented by the white line.*

3.2.3. Respiratory patterns extraction

Respiratory patterns are automatically extracted from diaphragm motion that is previously obtained. The extraction of respiratory patterns is only performed at the column *x* that has the largest diaphragm movement.

In general, a respiratory pattern consists of one peak and one valley. A semi-automatically peak and valley detection was proposed in [37]. Although this proposed method was able to detect peaks and valleys from a respiratory pattern, the respiratory signal is not obtained from time-sequential images. It is directly measured by a digital voltage signal using a pressure sensor. Moreover, manual user review is also required to verify the results.

In this study we propose an automatic peak and valley detection from respiratory signal obtained from diaphragm motion (Figure 3.3). We first perform noise filtering using an adaptive noise-removal filter [38]. Next step is to set a baseline value based on the statistical mode (most frequently occurring value) of the signal. A parameter, p is used to determine the height of the peak. Points in the respiratory signal that are higher than the baseline multiplied with p are marked as peak. The similar process is also done to detect the valleys. Instead of finding statistical mode, regional minima of the signal are calculated and multiplied by a parameter, v. All points below this value are marked as valley.

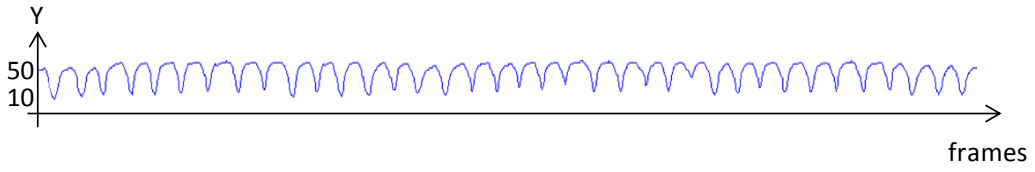

(a)

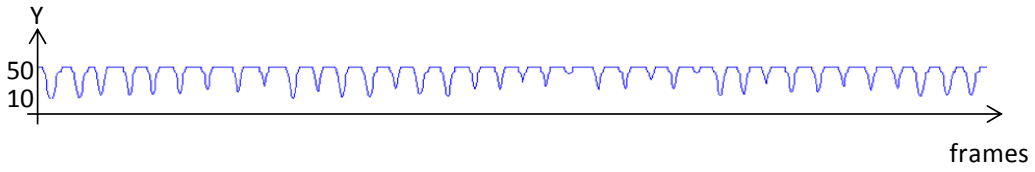

(b)

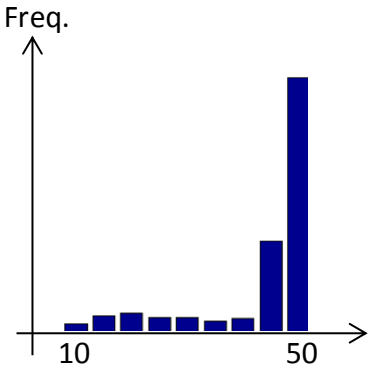

(c)

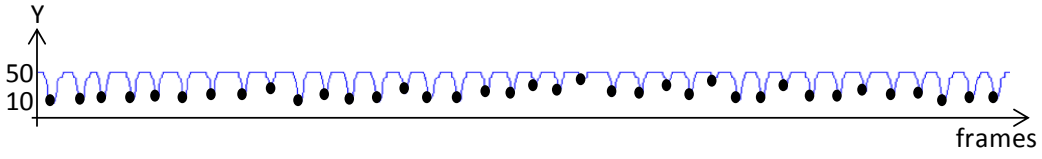

(d)

Figure 3. 3. Determining peaks from a signal. (a) Original signal before noise removal. (b) Signal after noise removal using an adaptive noise-removal filter. (c) Histogram of respiratory signal after noise removal; baseline is determined by most occurring value. Points that are higher than baseline multiplied a parameter p *are marked as peak. (d) Valleys are detected using regional minima. The detected valleys are circled.*

3.3. Results

We tested the proposed method to a total of 15 subjects (8 healthy volunteers and 7 COPD patients). The number of frame for each subject is 1200 frames. Table 3.1 shows the number of respiratory patterns found and the number frame for one respiratory cycle.

Table 3. 1. Number of respiratory patterns found and the average number of frame required for one respiratory cycle in healthy volunteers.

Subject	**# Resp. Pat.**	**#Frame/cycle**
Healthy Volunteers		
1	32	36.7
2	36	33.3
3	37	32.4
4	52	23.1
5	19	63.2
6	57	21.0
7	48	25.0
8	34	35.3
COPD patients		
1	49	24.5
2	77	15.6
3	34	35.3
4	38	31.6
5	61	19.7
6	56	21.4
7	46	26.1

Ideally, the number of frame for one respiratory cycle ranges from 25-35 frame/cycle. Figure 3.4 shows an example of respiratory patterns which successfully extracted from healthy volunteer #3. The number of detected respiratory patterns is 37

and the number of frame per cycle is 32.4 which is considered as normal respiratory motion.

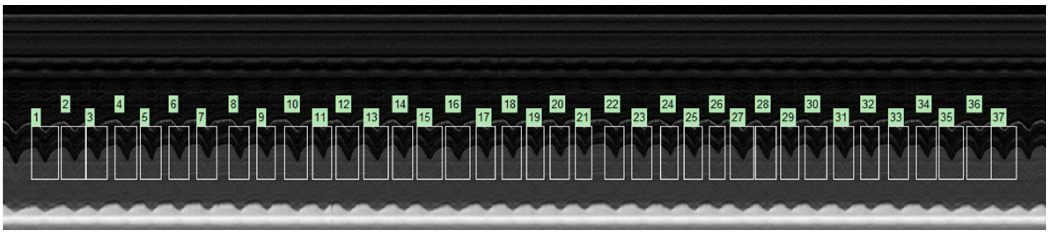

Figure 3. 4. Detected respiratory patterns for healthy volunteer #3.

However, breathing irregularity is a factor that makes respiratory pattern extraction failed. Another factor that affects the number of detected respiratory pattern is respiratory frequency. For example, subject 6 has the largest number of extracted respiratory patterns among the other healthy volunteers. The subject's 2D spatio temporal shows that this subject has high respiratory frequency (Figure 3.5a).

The healthy volunteer who has the smallest number of detected respiratory patterns is subject 5. As we can see in the Figure 3.5b, subject 5 has several irregular breathing cycles (pointed by white arrows) that make the system failed to extract them.

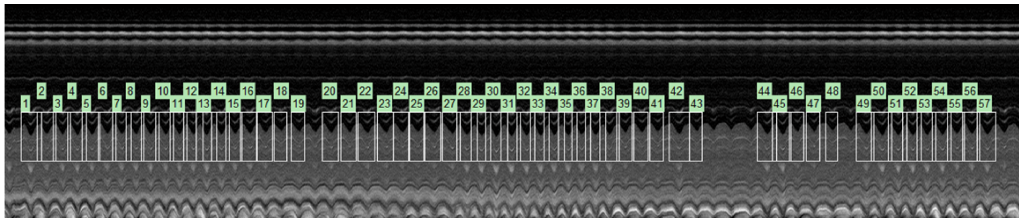

(a)

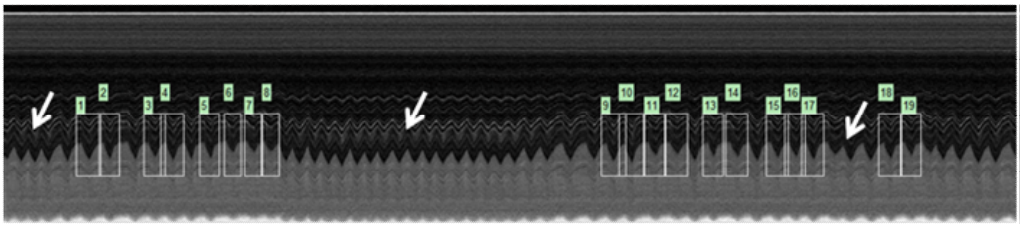

(b)

Figure 3. 5. An example of (a) high respiratory frequency and (b) irregular breathing of healthy volunteers

For COPD patients, the number of extracted respiratory patterns tends to be higher compared with healthy volunteers. Figure 3.6 shows two examples of COPD patients 5 and 6. The frame/cycle of these patients are 19.7 and 21.4, respectively. It indicates that these patients have smaller lung volume capacity compared with healthy subjects. Several irregular breathings were also found in the first 100 frames of the patient 6 (Figure 3.6b) and they failed to be extracted.

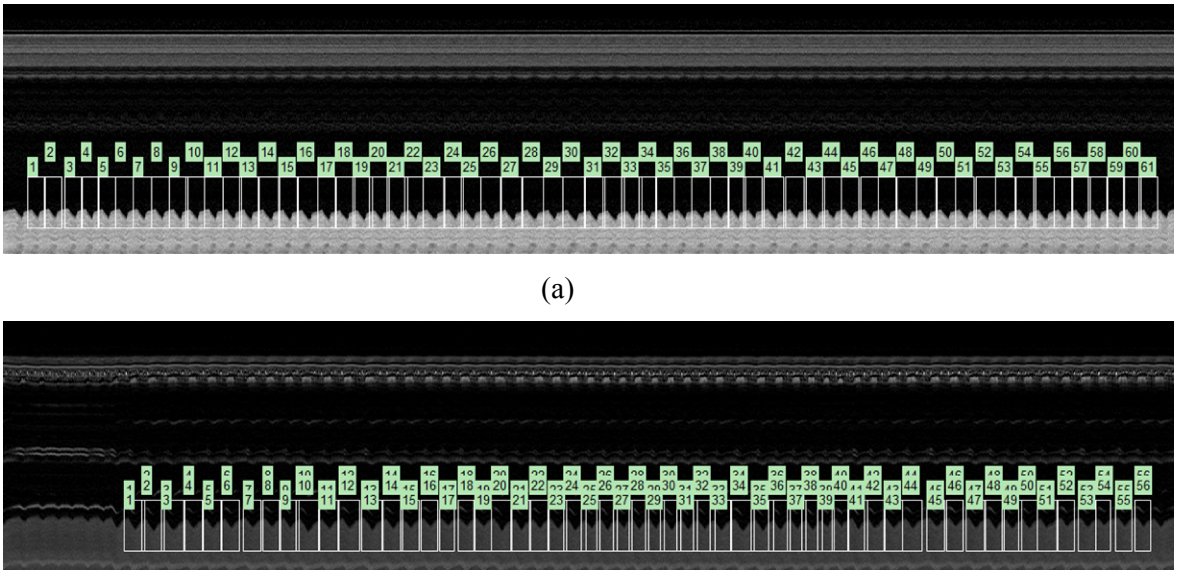

(a)

(b)

Figure 3. 6. Two examples of extracted respiratory patterns of COPD patient 5 and 6.

3.4. Conclusion

This study proposed an automatic method to extract diaphragm motion and respiratory patterns from time sequential MR images in sagittal plane. Our method successfully extracts diaphragm motion and respiratory patterns for both healthy volunteers and COPD patients. However, our study has certain limitations. First, it fails to detect irregular breathing patterns which can occur during MRI acquisition. Second, the results of the present study were obtained from a small number of subjects. Larger

number of subjects for both healthy volunteer and COPD patients are required to validate our method.

Acknowledgments

This study was supported in part by MEXT Kakenhi Nos. 22103504 and 24103703.

4

REDUCTION OF ACQUISITION TIME FOR 4D-MRI RECONSTRUCTION

Major parts of this chapter were published as a manuscript in the SPIE Journal of Medical Imaging:

W Swastika, Y Masuda, T Ohnishi et al.; "*Reduction of acquisition time in the intersection profile method for four-dimensional magnetic resonance imaging reconstruction of thoracoabdominal organs*," J. Med. Imag., 2(2), 024008 (2015) *)

*) *Used with the permission of the SPIE.*

Abstract

We have previously proposed an intersection profile method for reconstructing 4D-MRI consisting one breathing cycle of the thoracoabdominal region. This method captures a set of temporal sequence images in a proper sagittal plane and sets of temporal sequence images in continuous coronal slices. The former set is used as a navigator slice and the latter sets are used as data slices. A 4D-MRI is reconstructed by synchronizing the respiratory pattern found in the navigator slice and the data slices. In this study, we propose a prospective method to reduce the acquisition time for data slices. During data slice acquisition, the synchronization process between respiratory pattern found in the navigator slice and one data slice is monitored in real time. Data acquisition will be terminated and moved to the next data slice based on a threshold value. We used 14 data sets (7 patients with certain pulmonary disease and 7 healthy

volunteers) previously obtained for the original intersection profile method for a simulation using the proposed method to evaluate the time reduction and impact on image quality. Each of the data set was tested using 3 different threshold values and the acquisition time can be reduced up to 75%. Although the quantitative evaluation of image quality was slightly worse than by the conventional method, the difference based on the visual inspection was subtle to human eyes.

Keywords

4D-MRI, respiratory motion, intersection profile method, thoracoabdominal organs.

4.1. Introduction

Reconstruction of 4D-MRI using intersection profile method as described in section 1.2 is considered as a retrospective method. One of the drawbacks of retrospective method is that it requires long time to obtain a full data set. In this chapter we modify the method so as to shorten the acquisition time of MRI data. In the modified method, a reference respiratory pattern is determined from the navigator slice. Then, during the data slice image acquisition, each respiratory pattern is compared with the reference respiratory pattern in real time and a similarity measure between them is calculated. Once the similarity measure reaches the threshold, the image acquisition for the current data slice will be halted and the acquisition proceeds to the next position. In order to implement this idea to a real MRI equipment, manufacturer has to change the image acquisition system. Currently it is not realized yet. On the other hand, we have a lot of raw data collected from the previous method. So we can simulate how the prospective method works using those images.

In the following sections, we describe how we modified it to reduce the acquisition time. We then present the experimental results using 14 data sets. The time reduction and image quality are evaluated and discussed.

4.2. Modification to prospective method

The coordinate system, variables and image acquisition is same as we described in chapter 2. We modify the retrospective method in section 1.2 into a prospective method to reduce the time needed for DS acquisition. To find the best matching between respiratory patterns of NS and spatio temporal pattern of DS, structural similarity (SSIM) is used instead of NCC. SSIM index is measured by considering three important

components of image: luminance (mean), contrast (variance) and structure (cross-correlation) [39]. To measure SSIM of two images, *x* and *y*, the following SSIM function is used:

$$SSIM(x,y) = m(x,y)^{\alpha} \times v(x,y)^{\beta} \times c(x,y)^{\gamma}$$
$$= \left(\frac{2\mu_x\mu_y + C_1}{\mu_x{}^2 + \mu_y{}^2 + C_2} \right)^{\alpha} \times \left(\frac{2\delta_x\delta_y + C_1}{\delta_x{}^2 + \delta_y{}^2 + C_2} \right)^{\beta} \times \left(\frac{\delta_{xy} + C_3}{\delta_x\delta_y + C_3} \right)^{\gamma} \quad (4.1)$$

where μ_x and μ_y are mean value of image *x* and *y*; δ_x, and δ_y, denote the standard deviation of image *x* and *y*; and δ_{xy} denotes correlation coefficient. Three parameters α, β, and γ, are parameters to adjust component's contribution (usually set to 1) and constants C_1, C_2, and C_3 are small positive constants.

The use of SSIM is proven to be consistent with perceptual image distortion and works better than traditional similarity measures such as root mean square, normalized least square error, and correlation in term of maintaining image's structure [39] [40] [41].

Figure 4.2 shows a schematic illustration of the modified version of the intersection profile method. Here steps 6, 7 and 8 of the previous method are changed as shown below:

6'. Instead of using all respiratory patterns, choose one of the most frequent respiratory patterns from the NS and use it as a reference to compare with the corresponding respiratory patterns in the DS. The most frequent respiratory pattern is defined by a pattern that has the smallest mean distance from other respiratory patterns. We then determine the location of most frequent respiratory pattern as follows.

$$k'_{best} = \arg\min \Sigma^{m}_{\substack{j=1 \\ j \neq k}} \left\{ \Sigma_{z,t} \left(A_{j,\max}(z,t) - A_{k,\max}(z,t) \right)^2 \right\} \quad (4.2)$$

where m is the number of respiratory pattern found in the NS. The most frequent respiratory pattern is then defined as $A_{k'best,i}(z, t)$ where t ranges from $t_{k'best,i}$ to $t_{k'best,i}+w_{k'best,i}$.

In Eq. 4.2, $A_{j,i}$ represents the *j-th* respiratory pattern in intersection location *i,* where j ranges from $1..m$ and i ranges from $1..n$. We can see $A_{j,i}$ in Figure 4.1 as a box with certain width and height. The z and t in Eq. 5. 4 represent the "height" and "width" of the box (respiratory pattern). Therefore, the range of t is limited by the width of the box.

Note that the location to pick most frequent respiratory pattern is the intersection location that has the largest diaphragm movement. To obtain the intersection location that has the largest diaphragm motion, we measured the displacement of the diaphragm for each intersection location from end inhalation to end exhalation (automatically) and determine the intersection location that has the largest displacement (denoted as y_{max}).

Once the position of the most frequent pattern (k'_best) at y_{max} was obtained, the same position is used for other intersection locations ($y_1..y_n$). Thus, the position of k'_best is always the same for each intersection location. Another reason why k'_best is picked at only one intersection location rather than picked at each intersection location is that different k'_best that is picked at each intersection location might produce "out-of-phase" reconstruction since the respiratory patterns ($1..m$) might have different size.

7'. For y_i, i=1, 2, 3, ...n, evaluate the SSIM value between $A_{k'best,i}$ and B_i as image acquisition of DS proceeds. When the SSIM value becomes greater than a predetermined value, stop the data acquisition in the current position (y_i) and

proceed to the next intersection position.

During the coronal slices acquisition, the signal of MR image is also processed simultaneously. The processing includes: (1) calculate similarity measure between respiratory pattern in sagittal plane and coronal plane, (2) save the data if it satisfies the condition (similarity measure higher than the threshold value) and (3) store the best matching image into storage for reconstruction purpose. The detail of time required for the image processing is shown in fig. 4.1.

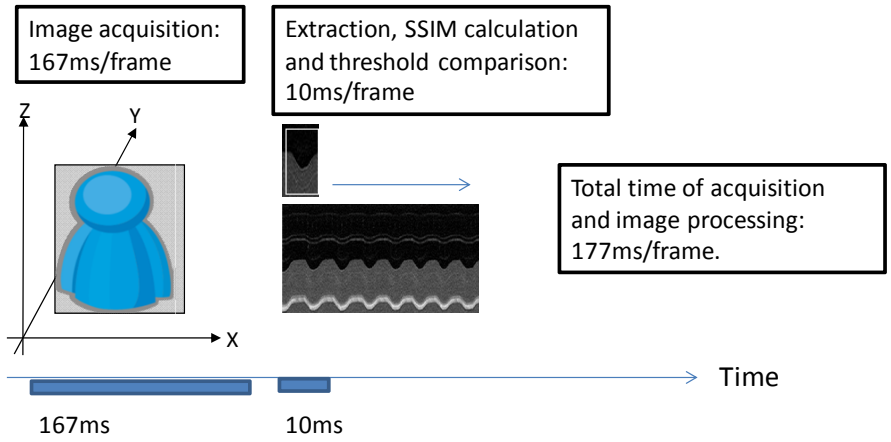

Figure 4. 1. Time required to acquire and process the image.

8'. Reconstruct the 4D-MRI by combining DS $f_{data}(x, y_i, z, t_{data})$ where t_{data} ranges from $t_{k'best,i}$ to $t_{k'best,i}+w_{k'best,i}$.

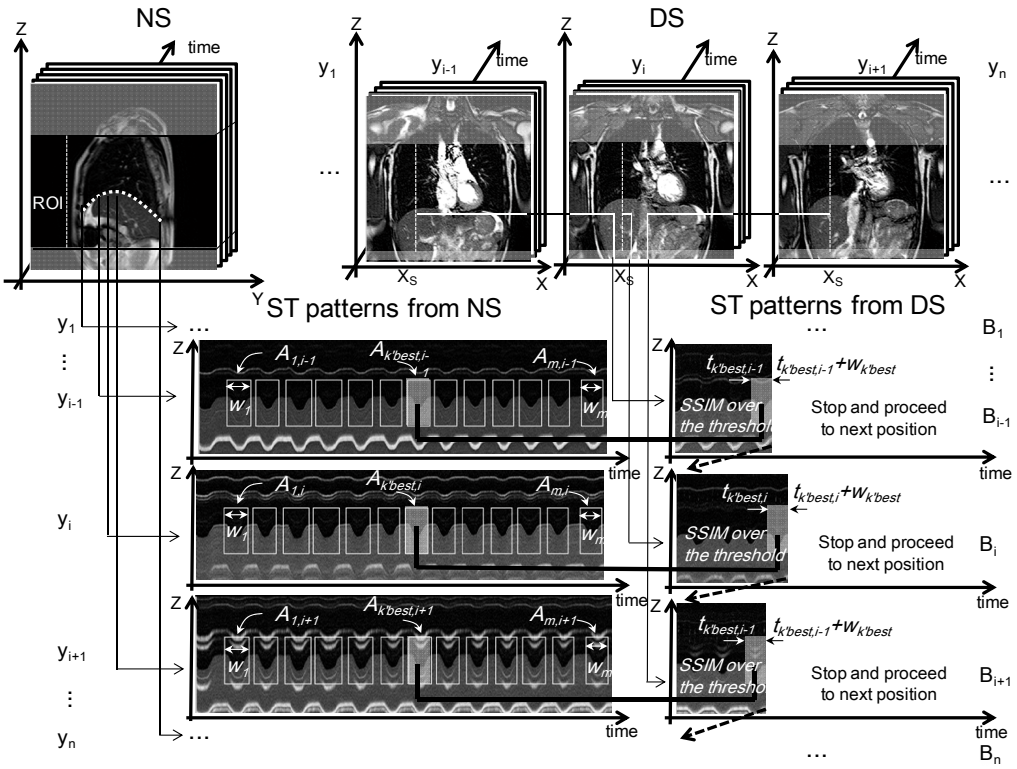

Figure 4. 2. Modification to prospective method. The acquisition is stopped and proceed to the next data slice once the SSIM value higher than the threshold value

Fixed threshold is used to implement 4D-MRI reconstruction using the prospective method. It sets a certain threshold which will be used to stop the acquisition process if the SSIM value exceeds it. The SSIM value has an influence to the image quality of 4D-MRI. In this study, three threshold values 0.5, 0.4, and 0.3 are investigated.

There are no precise rules for selecting SSIM value to evaluate image quality or compare between two images [42]. As proposed in [39], SSIM value is very sensitive to structural changes on the image. Therefore, a small distortion on the image will produce low SSIM value. In [39], the author show that SSIM value of JPEG compressed image, blurred image and salt-pepper noise are is 0.6949, 0.7052 and 0.7748. SSIM higher than 0.9 can only be achieved by contrasts-stretched and mean-shifted image – which means there are no structural changes in the image structure.

Several studies have also been proposed to assess the quality of medical images using SSIM (specifically MR image) [43] [44]. In [43], the authors show the quality assessment performance of compressed MRI images using SSIM. The range of SSIM value between original image and compressed MR images is 0.195 to 0.8234. Apparently, achieving SSIM higher than 0.9 is difficult to obtain when distortion occurred on the image.

Similar SSIM values are also achieved in our study. By comparing respiratory pattern from the navigator slice and data slice using SSIM, the range falls between 0.1 to 0.7. Based on our empirical SSIM values during the matching process, we set the threshold values to 0.3, 0.4 and 0.5.

4.3. Experiment

4.3.1. Image data used in experiment

The MR images were acquired using 1.5T INTERA ACHIVA nova-dual (Philips Medical Systems) whole-body scanner with a 16ch SENSE TORSO XL coil. A 2D balanced FFE sequence was used. The imaging parameters were as follows: SENSE factor, 2.2; flip angle, 45^{o}; TR, 2.2ms; TE, 0.9ms; FOV, 384mm; in-plane resolution, 256x256 pixels and 1.5x1.5mm^2; slice thickness, 7.5mm; slice gap, 6.0mm; scan time, 150ms/frame. All subjects were instructed to breath normally during the acquisition process. The image acquisition experiment was conducted under the approval of the Ethical Review Board of Chiba University. The software used to implement our method was MatLab 7.10 and we ran it on a PC with Intel®Core™2 Quad, 2.66GHz, 16GB RAM. Total processing time for one subject to complete the 4D-MRI reconstruction after obtaining a set of raw data was less than one minute.

Fourteen subjects (seven healthy subjects and seven patients with known pulmonary diseases) participated in this study. The number of DSs varied from 14 to 25 slices where each slice contained 400 frames. The number of NS frames also varied from 400 to 1200. Statistical data for the subjects are summarized in Table 4.1.

Table 4. 1. Subjects' data statistic. For each subject, the number of slice of DS, number of frame of NS, and diagnosis are given

Subj.		#DS	# NS' frame	Diagnosis
VOLUNTEER	V1	20	400	-
	V2	24	800	-
	V3	24	800	-
	V4	14	1200	-
	V5	14	1200	-
	V6	13	1200	-
	V7	13	1200	-
PATIENTS	P1	14	1200	Pulmonary Tumor
	P2	25	1200	COPD
	P3	23	1200	Right-giant bulla
	P4	10	1200	COPD
	P5	25	1200	COPD
	P6	12	1200	COPD
	P7	12	1200	COPD

The number of frames of NS varies only for the volunteers (healthy subjects). During the acquisition, when the breathing patterns of the subjects are considered as a regular breathing, the acquisition does not have to be 3 min long. One or two min should be enough to get the variation of the breathing patterns from the subjects. In most cases, healthy volunteers have regular respiratory patterns. When the operator does not spot any irregular breathing within one min, he stops the acquisition in one min. However, if there seems to be an irregular breathing within one min, the acquisition will

be continued for another one min. For the patients, some of them have irregular breathing patterns and the acquisition time has to be 3 min long to capture the breathing patterns' variation.

4.3.2. Time reduction using a predetermined threshold value

As described earlier, by applying the retrospective method, DS acquisition time by minutes is equivalent to the number of slices. Time reduction is possible using the prospective method that employs a predetermined threshold value. During the DS acquisition, when the SSIM value in the y_i position is larger than the threshold value, the acquisition process will be stopped and the process will proceed to the next slice position.

By applying smaller threshold value, better time reduction can be achieved. Complete comparison of time reduction is shown in Table 4.2. Here "w/o T" stands for "without threshold" that the modified method is applied without thresholding. The total acquisition time for volunteer data can be reduced by 23.1%, 53.1% and 75.6% on average for 0.5, 0.4 and 0.3 threshold values, respectively. For patient data, the average of time reduction are 32.5%, 59.3% and 84.0% for 0.5, 0.4 and 0.3 threshold values.

Table 4. 2. Comparison of total acquisition time and time reduction of w/o T, 0.5, 0.4 and 0.3 threshold values.

Subj.		w/o T	0.5		0.4		0.3	
		Total DS acquisition time	Total DS acquisition time	Time reduction (%)	Total DS acquisition time	Time reduction (%)	Total DS acquisition time	Time reduction (%)
Volunteers	V1	20:00	17:57	10.3	14:14	28.8	3:01	84.9
	V2	24:00	5:14	78.2	2:05	91.3	1:36	93.3
	V3	24:00	15:08	36.9	7:06	70.4	4:11	82.6
	V4	14:00	10:20	26.2	5:33	60.4	4:05	70.8
	V5	14:00	12:39	9.6	8:07	42.0	6:17	55.1
	V6	13:00	10:14	21.3	6:45	48.1	4:35	61.8
	V7	13:00	10:07	22.2	6:10	52.6	2:27	81.2
Geomean		**16:49**	**10:58**	**23.1**	**6:18**	**53.1**	**3:26**	**75.6**
Patients	P1	14:00	8:46	37.4	4:53	65.1	1:55	86.3
	P2	25:00	19:51	20.6	11:14	55.1	4:06	83.6
	P3	23:00	6:40	71.0	2:15	90.2	1:42	92.6
	P4	10:00	6:12	38.0	2:41	73.2	1:43	82.8
	P5	25:00	17:02	31.9	10:26	58.3	6:30	74.0
	P6	12:00	8:28	29.4	5:50	51.4	2:14	81.4
	P7	12:00	9:38	19.7	7:38	36.4	1:24	88.3
Geomean		**16:10**	**9:59**	**32.5**	**5:30**	**59.3**	**2:24**	**84.0**

The quality of the 4D-MRI reconstructions were also assessed by the geomean of all the best SSIM values between the reference spatio-temporal image of the NS and spatio-temporal image of the DSs at all intersection locations. Figure 4.3 shows the plot of geomean of SSIM and time reduction. Overall results indicated that the best geomean of the SSIM was achieved by the w/o T method.

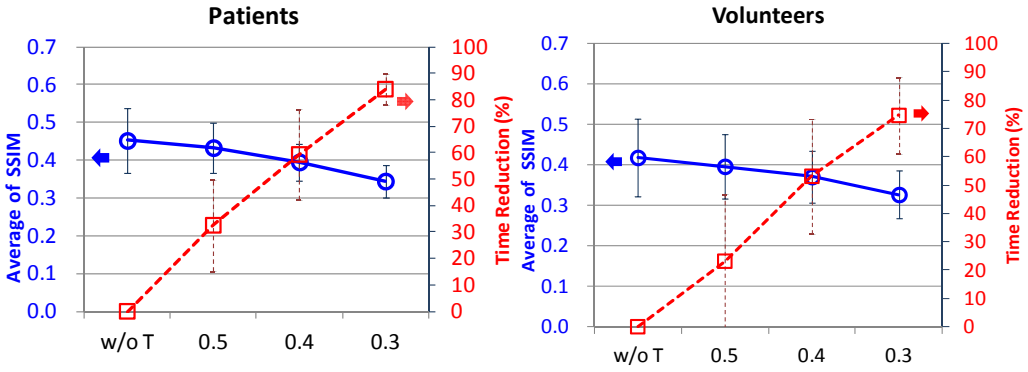

Figure 4. 3. Average of SSIM and data slice time reduction of volunteers and patients. Solid line indicates the average of SSIM (left scale) and dashed line indicates time reduction (right scale).

Certain threshold values used in reconstruction reduced the DS acquisition time in the exchange of the lower SSIM geomean (or in other words, lower quality of the 4D-MRI reconstruction). Both volunteer and patient data results demonstrated that 0.4-0.5 threshold value may reduce data acquisition time up to 50%. Reconstructing 4D-MRI using higher threshold value, for example 0.6, is also possible. However, the time reduction in this scenario would be very small since most data slices have SSIM values less than 0.6.

The trade-off of time reduction is the quality of 4D-MRI reconstruction. Image quality of 4D-MRI is discussed in the next section. Visual evaluation is first discussed and followed by the quantitative evaluation.

4.4. Image quality evaluation

4.4.1. Visual Evaluation

4.4.1.A. Volume rendering image and MIP image of reconstructed 4D-MRI

Reconstructed 4D-MR images were visualized by a volume rendering technique implemented in Osirix. Three images of 4D-MRI reconstruction from the same subject

(V1) are shown in Figure 4.4. Fig. 4.4a, b, and c show the reconstruction using the retrospective method, the prospective method w/o T, and the prospective method with 0.3 threshold value, respectively. End inhalation phase is shown in the left side and end exhalation is shown in the right side of Fig. 4.4. In order to show the difference between left and right images, we drew a white dashed line at the top level of the diaphragm of the left image. The total time required to obtain whole data set of 4D-MRI using the retrospective method and the prospective method w/o T were 24 min (4 min to obtain navigator slice and 21 min to obtain data slices). By using the prospective method with 0.3 threshold value, the total data slice acquisition time can be reduced to 3 min 1 s. From the visual inspection, we confirmed that these volume rendering images look very similar.

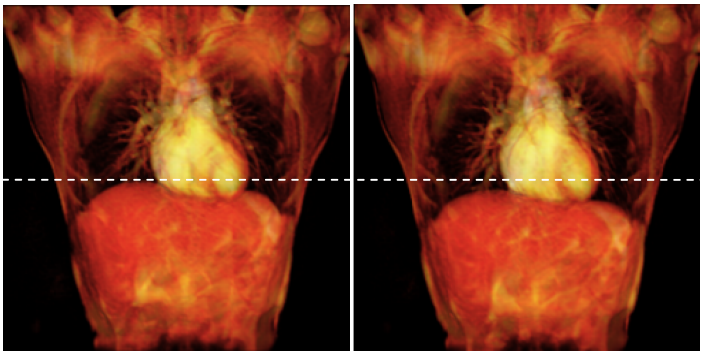

(a) Retrospective method

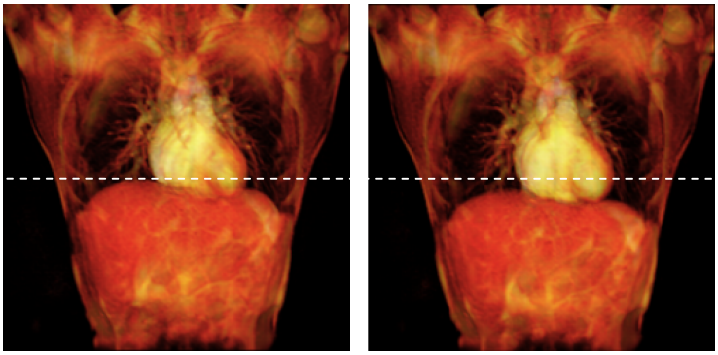

(b) Prospective method w/o T

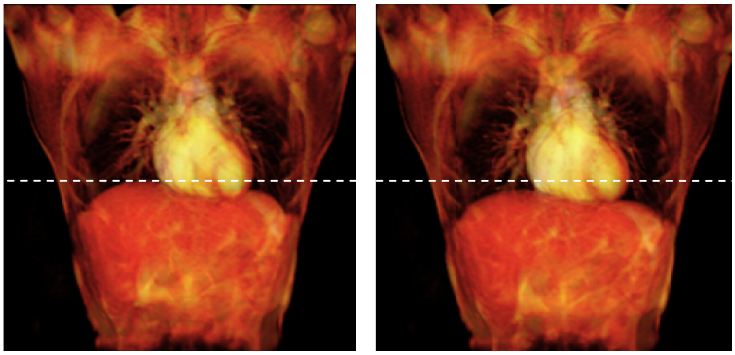

(c) Prospective method with 0.3 threshold value

Figure 4. 4. Examples of two different phases after volume rendering of V1 using Osirix. (a) Reconstructed using the retrospective method, total time of data acquisition was 24 min; (b) Reconstructed using the prospective method w/o T, total time of data acquisition was 24 min; (c) reconstructed using the prospective method with 0.3 threshold value, the total time of data acquisition was 3 min 1 s (84.9% time reduction).

Another visual evaluation of reconstructed 4D-MRI of V1 was also performed using maximum intensity projection (MIP) [18]. We compared the MIP images of 4D-MRI between the retrospective and the prospective method. Fig. 4.5a, b and c show the MIP images of the reconstruction using the retrospective method, the prospective method w/o T, and the prospective method with 0.3 threshold value, respectively. As shown in the figure, these MIP images also look similar.

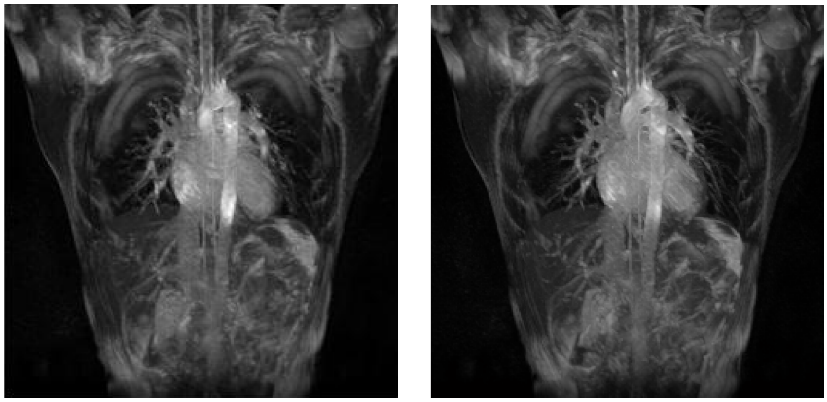

(a) Retrospective method *(b) Prospective method w/o T*

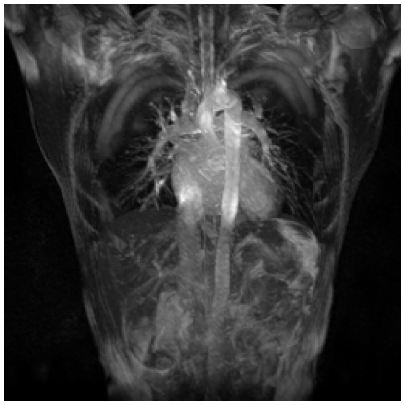

(c) Prospective method with 0.3 threshold value

Figure 4. 5. Three MIP images of reconstructed 4D-MRI of V1. (a) Reconstructed using the retrospective method, (b) reconstructed using the prospective method w/o T, and (c) reconstructed using the prospective method with 0.3 threshold value.

4.4.1.B. Sagittal slice evaluation

The shape of diaphragm extracted from 4D-MRI in sagittal plane can also be used as an indicator of reconstruction quality. We extracted a sagittal cut at NS location X_s and another sagittal cuts at two locations different from NS as shown in Fig. 4.6. The distances between the sagittal cuts and original location of NS were 30mm on the left side (X_s-30mm) and 30mm on the right side (X_s +30mm).

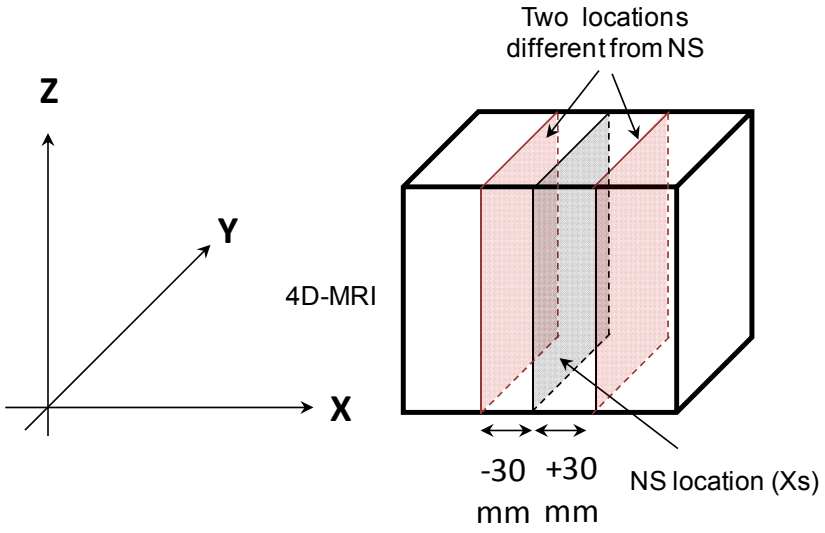

Figure 4. 6. Extraction of sagittal cuts from reconstructed 4D-MRI. The distances of the extracted sagittal cuts are 30mm on the left side and 30mm on the right side of original NS position.

The visual comparison of extracted sagittal cuts at the same location as NS and two locations different from NS are shown in Fig. 4.7. We picked one volunteer and two patients who have 20 slices or more as examples and 4D-MRI reconstruction using the retrospective method, the prospective method w/o T and the prospective method with 0.3 threshold value. Figure 4.6 shows sagittal cuts extracted from the V1, P2 and P3.

Only at the location of the original NS (X_s), we can compare the appearance of the original NS image and sagittal cuts extracted from the reconstructed 4D-MRI. Since the number of DSs is limited and the spatial resolution of the sagittal cuts is low, the

sharpness of the sagittal cuts is clearly lower than the original NS images. However, the general structure was natural and similar to that of the original NS image. The diaphragm boundary of sagittal cuts from the retrospective method and the prospective method w/o T were found to be smoother compared to 0.3 threshold. The diaphragm shape of 0.3 threshold had more crease over the boundary (indicated by white arrow). The quantitative evaluation of such comparison will be discussed in the Sec. 4.4.2.

The sagittal cuts extracted from X_s-30mm and X_s +30mm of NS location have a similar image quality to the sagittal cut at X_s. However, vertical stripes are visible especially in P2 case. Pixel value adjustment should be done to achieve the uniformity of intensity. However, in any sagittal cuts, the diaphragm is clearly separable with other organs and the shapes look natural.

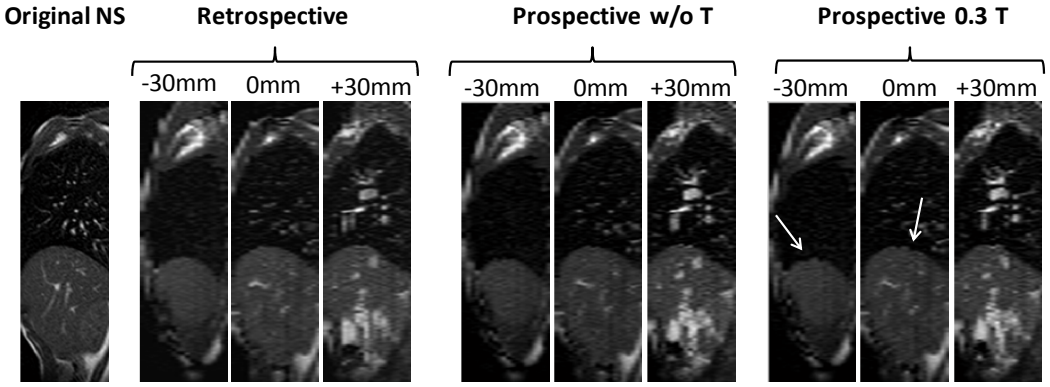

(a) V1

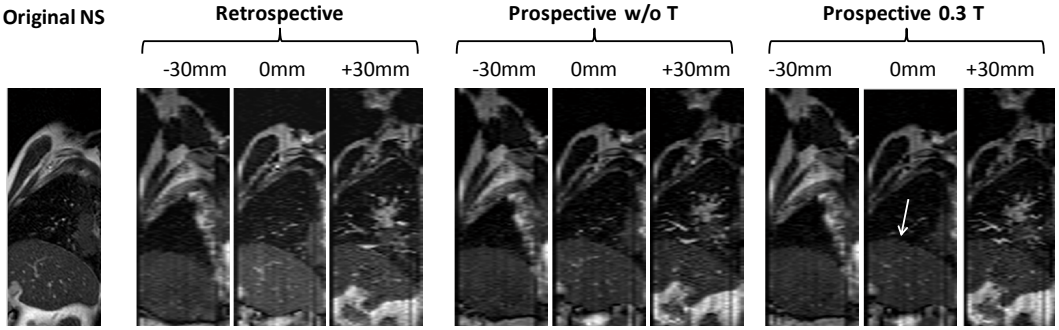

(b) P2

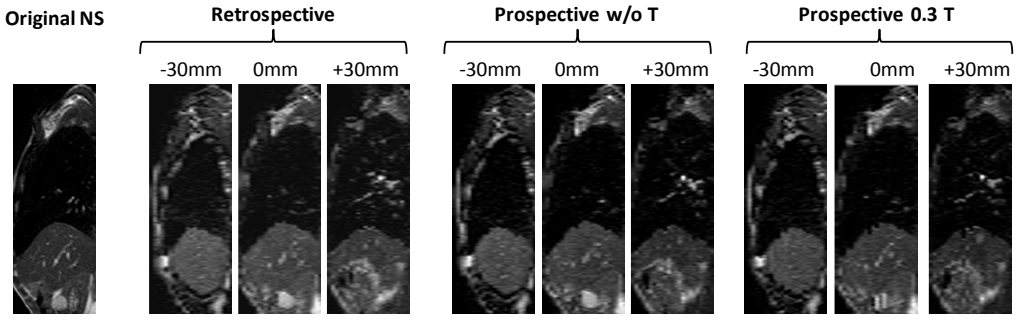

(c) P3

Figure 4. 7. Visual comparison of original NS and sagittal cuts extracted from location of NS (X_s) and two locations different from NS (X_s-30mm and X_s+30mm). The sagittal cuts were extracted from the retrospective method, the prospective method w/o T and the prospective method with 0.3 threshold value. White arrow indicates crease over the diaphragm boundary.

4.4.2. Image quality evaluations

Focusing on the sagittal cut of 4D-MRI corresponding to the NS, we performed two validation experiments to assess the accuracy of the prospective 4D-MRI reconstruction using 0.5, 0.4 and 0.3 threshold values, respectively. We defined the sagittal slice from NS as a ground truth and evaluate the sagittal cuts in the NS location from the 4D-MRI.

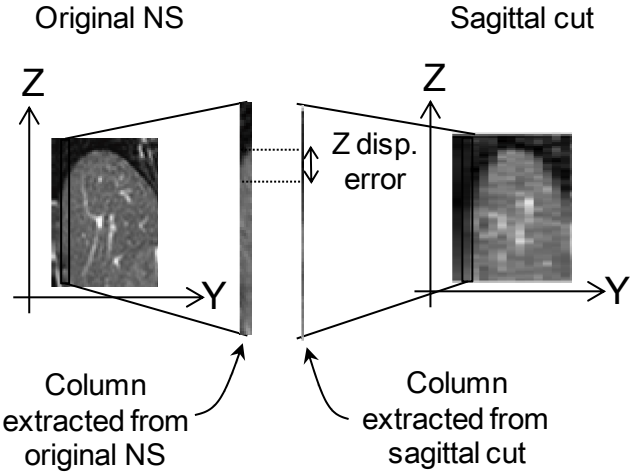

Figure 4. 8. Displacement error of diaphragm measured based on the difference diaphragm boundary position between the sagittal slice from NS as ground truth and sagittal cuts from reconstructed 4D-MRI.

In the first validation, the measurement was performed by calculating the difference of the Z axis displacement at the intersection location (y_i, i=1, 2, 3, ..., n). The schematic diagram how to measure the Z displacement error is shown in Figure 4.7. Each column of the sagittal cut in the intersection location (y_i, i=1, 2, 3, ..., n) was extracted. In general, the pattern of the extracted column consists of two major intensities, dark and gray. The extracted column of sagittal cut is then matched using cross correlation along the Z axis with the corresponding column of the original NS. Z displacement error is determined from the position of the best cross correlation value. Ideally, the extracted column of sagittal cut has the same pattern as the extracted column of original NS along the intersection location. Thus, the Z displacement errors

along the intersection location are equal to 0 and the diaphragm shape of sagittal cut is also same as the navigator slice. However, since our method tries to find the best matching of the respiratory pattern between navigator slice and data slice, such ideal condition is difficult to obtain. Therefore, in the first validation, we calculate the average of the Z differences over intersection locations (y_i, i=1, 2, 3, ..., n) and respiratory phases (frames).

In the second validation, we compare the similarity of the sagittal cuts extracted from the reconstructed 4D-MRI with the original NS. The similarity measure is done using cross correlation function. We used NCC since contrast variation between the NS and DS may have been present. Higher NCC indicates that the diaphragm structure extracted from 4D-MRI is moving synchronously with the original NS.

Table 4.3 shows the results of two validation experiments; one is Z displacement error (in mm) and the other is geomean of NCC. The geomean of NCC is also shown in Figure 4.9.

Table 4. 3. Comparison of Z displacement error of diaphragm and geomean of NCC of w/o T, 0.5, 0.4 and 0.3 threshold values.

Subj.		**w/o T**			**0.5**			**0.4**			**0.3**		
		Z disp. error (mm)		Geo -mean of NCC	Z disp. error (mm)		Geo-mean of NCC	Z disp. error (mm)		Geo-mean of NCC	Z disp. error (mm)		Geo-mean of NCC
		Mean	SD		Mean	SD		Mean	SD		Mean	SD	
Volunteers	V1	2.51	0.24	0.85	2.56	0.26	0.85	2.63	0.37	0.84	2.60	0.33	0.83
	V2	2.32	0.53	0.86	2.39	0.55	0.84	2.71	0.72	0.82	2.94	0.89	0.81
	V3	2.46	0.47	0.80	2.83	0.68	0.79	3.14	0.75	0.78	3.62	0.82	0.75
	V4	3.06	1.12	0.85	3.13	1.17	0.84	3.27	1.23	0.84	3.36	1.29	0.83
	V5	2.56	0.72	0.73	2.61	0.81	0.73	2.83	0.83	0.73	3.05	0.89	0.72
	V6	2.98	1.00	0.67	3.27	1.14	0.67	3.39	1.27	0.66	3.03	1.38	0.66
	V7	2.52	1.17	0.80	2.48	1.17	0.80	2.62	1.22	0.80	2.43	1.33	0.79
Mean		**2.63**	**0.75**	**0.79**	**2.75**	**0.83**	**0.79**	**2.94**	**0.91**	**0.78**	**3.00**	**0.99**	**0.77**
Patients	P1	3.01	0.71	0.79	3.04	1.06	0.78	3.01	1.28	0.78	2.90	1.26	0.76
	P2	2.34	0.43	0.63	2.33	0.47	0.63	2.29	0.61	0.62	2.30	0.70	0.61
	P3	3.65	0.89	0.89	4.45	0.94	0.87	4.51	1.07	0.85	4.26	0.83	0.83
	P4	4.44	0.67	0.92	4.28	0.62	0.92	4.28	0.96	0.92	4.16	1.05	0.89
	P5	2.67	0.35	0.84	2.73	0.37	0.83	2.70	0.42	0.83	2.58	0.40	0.83
	P6	2.75	1.31	0.81	2.78	1.30	0.80	2.81	1.36	0.80	3.22	1.28	0.80
	P7	2.55	0.78	0.87	2.58	0.82	0.86	2.73	0.90	0.86	3.02	1.20	0.86
Mean		**3.06**	**0.73**	**0.82**	**3.17**	**0.80**	**0.81**	**3.19**	**0.94**	**0.81**	**3.21**	**0.96**	**0.80**

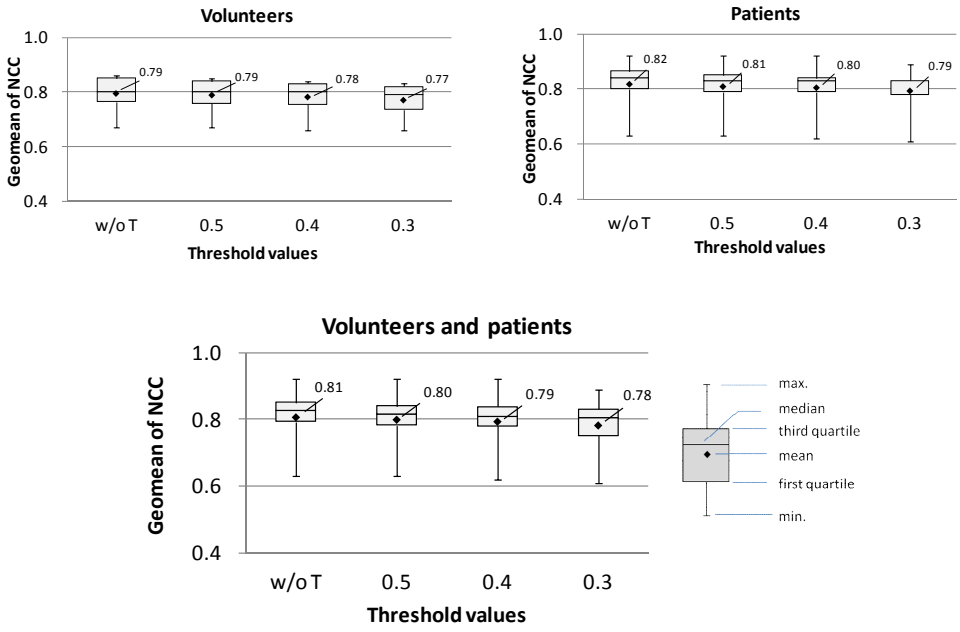

Figure 4. 9. Range and distribution of geomean of NCC of volunteer, patients and all. The differences of geomean of the NCC between w/o T, 0.5, 0.4, and 0.3 threshold values were small for both volunteers and patients..

The averages of the geomean of NCC for volunteers were 0.80, 0.79, 0.78, and 0.77 for w/o T, 0.5, 0.4, and 0.3 threshold values, respectively. For the patients, the averages were 0.82, 0.81, 0.81 and 0.80 for w/o T, 0.5, 0.4, and 0.3 threshold values. The differences were very small which indicates that the reconstruction using w/o T, 0.5, 0.4 and 0.3 threshold values were similar.

Figure 4.9 shows the range and distribution of Z displacement error when all errors pooled in one distribution. The maximum errors for volunteers were 8.0mm, 8.0mm, 9.0mm, and 9.0mm for w/o T, 0.5, 0.4, and 0.3 threshold values, respectively. For patients, the maximum errors were 8.0mm, 8.0mm, 8.0mm, and 9.0mm for w/o T, 0.5, 0.4, and 0.3 threshold values, respectively.

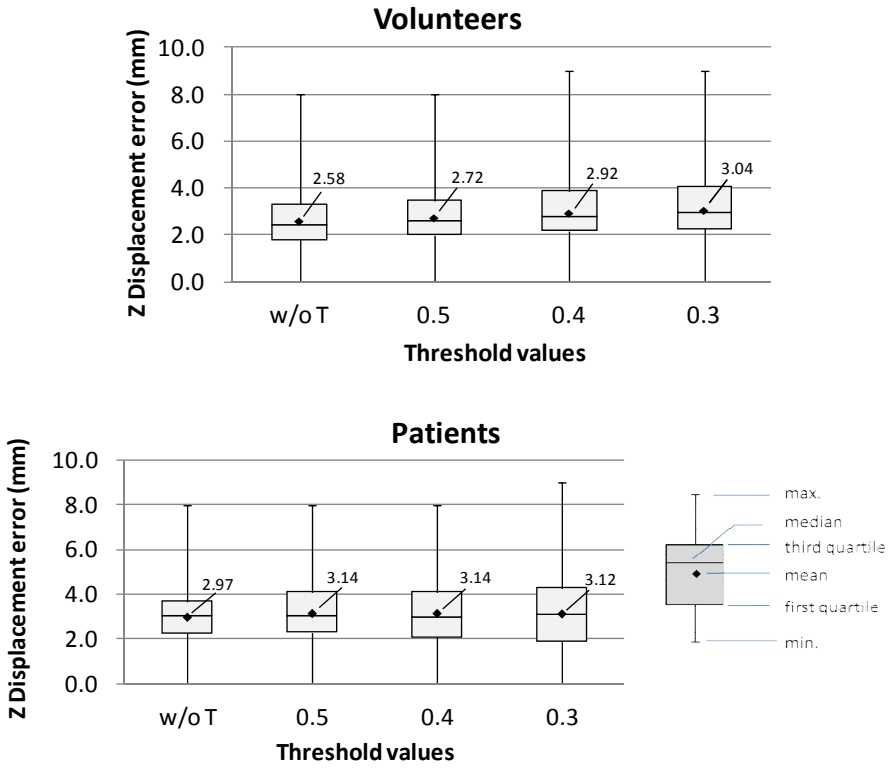

Figure 4. 10. Range and distribution of Z displacement error of diaphragm of (a) volunteers and (b) patients after pooling all errors into one distribution.

Assuming the Z displacement errors pooled in one distribution for volunteers and patients are normally distributed, interval and range of 95% confidence level is listed in Table 4.4.

Table 4. 4. Corresponding interval and range of 95% confidence level after pooling Z displacement errors into one distribution.

Subj.	**w/o T**		**0.5**		**0.4**		**0.3**	
	Interval (mm)	Range (mm)	Interval (mm)	Range (mm)	Interval (mm)	Range (mm)	Interval (mm)	Range (mm)
Volunteers	±0.26	2.32-2.84	±0.27	2.45-2.98	±0.28	2.64-3.20	±0.28	2.75-3.32
Patients	±0.25	2.72-3.21	±0.28	2.86-3.42	±0.28	2.86-3.42	±0.28	2.83-3.40

4.5. Discussion

In this study, we implemented a fixed threshold using SSIM for our prospective method to reconstruct a 4D-MRI consisting one breathing cycle. The main purpose of implementing the prospective method is to reduce acquisition time of the data slices. In the cases when all SSIM values were lower than the threshold value, maximum acquisition time will be required. Also when most of SSIM values were lower than the threshold value, the time reduction was very small.

Reconstruction using 0.5 threshold value for V5, for example, showed that the total data slice acquisition time was 12 min 39 s, which was reduced by only 1 min and 11 s (reduced by only 9.6%) compared to V2 which demonstrated an 18 min (78.2%) reduction using the same 0.5 threshold value. Only 9.6% time reduction was observed in V5 because most of the SSIM values in the intersection location were found to be lower than the threshold. As a result, full acquisition time, 1 min, were required in the most DSs.

We validated the 4D-MRI reconstruction visually and quantitatively. The visual validation includes MIP volume rendering and comparison of sagittal cuts between original NS and sagittal cuts extracted from 4D-MRI. Since the 4D-MRI is composed of a stack of coronal images captured, the thickness of the coronal image determines the resolution of the sagittal cut. Currently the slice thickness is 7.5mm and it is hard to improve this resolution markedly. When the thickness is lowered, for examples to 3.0mm or 4.0mm, the signal-to-noise ratio becomes worse. Consequently, the image quality will also be degraded. Even if possible, the acquisition of many more DSs is needed. It does not meet the aim of time reduction. In spite of lower resolution of the sagittal cuts, the diaphragm shape of the sagittal cuts in Figure 4.7, extracted from

X_s-30mm, X_s, and X_s+30mm of NS location, are clearly separable with other organs and the shapes look natural.

The first quantitative validation was performed by measuring the displacement error of diaphragm. Mean of Z displacement error using w/o T, 0.5, 0.4 and 0.3 threshold values was smaller than 5mm. The standard deviation was also found to be small, which indicates that the displacement error in each respiratory phase is close to the mean.

The second quantitative validation was carried out by comparing the similarity of sagittal cuts from reconstructed 4D-MRI with the NS as the ground truth. As shown in Figure 4.9, the differences of geomean of the NCC between w/o T, 0.5, 0.4, and 0.3 threshold values were small for both volunteers and patients. Thus, the quality of reconstruction using threshold method was very similar with the ground truth and in the same time, the total data acquisition can be reduced up to 75%.

The geomean of NCC for P2 was found to be smallest among the others. Figure 4.11 shows the sagittal cuts extracted from reconstructed 4D-MRI and the original NS of P2. In the bottom left of the original NS, white region supposed to be fat was clearly observed. On the other hand, the bottom left of the sagittal cut showed an unclear white region. Although the exact reason of this difference is unclear to us, the difference of spatial resolution could be a possible reason. This difference mainly seems to reduce the NCC value. However, the diaphragm surface from the sagittal cuts was also similar as the original NS. In fact, the displacement error was less than 3mm from Table 4.3.

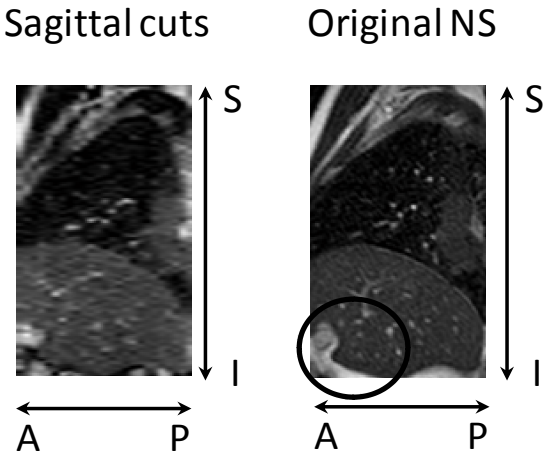

Figure 4. 11. Comparison of sagittal-cuts extracted from reconstructed 4D-MRI and original NS of patient P2.

As shown in the table 4.3, the Z displacement errors of diaphragm motion are 3.06±0.75mm and 2.63±0.75mm for patients and volunteers, respectively. For diaphragm motion, the error is clinically acceptable (<1cm) [45]. However, for other clinical applications that required high precision such as modeling respiratory motion for image guided intervention or radiation therapy, the mean error is too large. Keal et al suggested that the error should less than 3mm to be clinically acceptable [1]. Therefore, our proposed method is not suitable and a more accurate reconstruction method is required. The CT image is probably more appropriate for respiratory modeling since CT image has higher imaging resolution and less motion artifact which leads to better accuracy for 4D imaging reconstruction.

It is also interesting that the time reduction of the patients is higher compared to the volunteers. Time reduction is related with displacement of diaphragm to certain degree. During the matching process, if the displacement is small, the time reduction tends to be high. On the other hand, if the displacement is large, the time reduction tends to be low. The figure below shows the correlation between time reduction and diaphragm displacement.

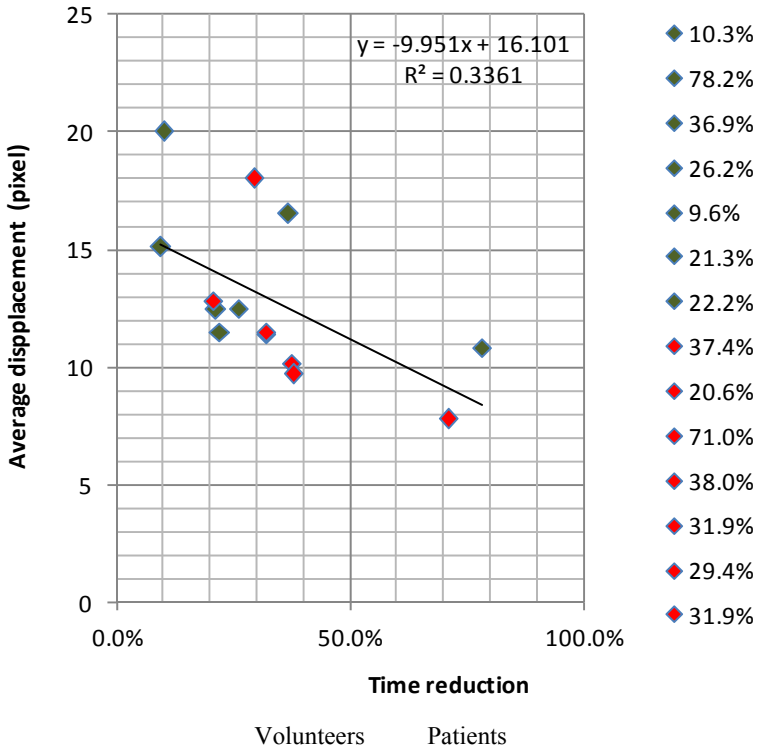

Figure 4. 12. Correlation between time reduction and average displacement of diaphragm.

Apparently, small displacement of the diaphragm is one of the factor to achieve high SSIM value during the matching process. Therefore, the SSIM will soon reach the threshold value and the acquisition for current frame is stopped. As a result, the time reduction for current frame is high.

Finally, we introduce one application of 4D-MRI briefly. In [46], we demonstrated how to extract the diaphragm motion from 4D-MRI. The advantage of using 4D-MRI to extract diaphragm motion is that both diaphragm surface and motion can be captured. We then analyzed and compared displacement map that is derived from the diaphragm motion of healthy volunteers and COPD patients. Using the displacement map, we found that COPD patients tended to have smaller displacements in certain area compared to healthy volunteers. We were also able to locate paradoxical motion of the diaphragm which is one of the COPD characteristics. Such information obtained from

4D-MRI will be beneficial for the physician and leads to a better treatment for COPD. In such an application, the above mentioned stable extraction of diaphragm was very useful.

4.6. Conclusion

We have improved the intersection profile method proposed previously to reconstruct 4D-MR images. We carried out a prospective 4D-MRI reconstruction to shorten acquisition time. Although the prospective synchronization method was tested only in simulations using previously acquired full data sets, we found that the prospective methods with 0.3 threshold value successfully reduced acquisition time of data slices by 75.6% and 84.0% for volunteer and patient data.

The quality of the 4D-MRI reconstruction was visually evaluated in three aspects; volume rendering, MIP images, and sagittal cut images. In most cases, the image quality of prospective reconstruction of 4D-MRI was satisfactory. The quality of the 4D-MRI reconstruction was also validated by calculating the displacement of diaphragm and calculating the geomean NCC value between the reconstructed 4D-MRI and the original navigator slice.

One limitations in full-scale implementation of this method is the need for significant modification in the manufacturing of MR scanner system. However, upon implementation of this method, it is reasonable to expect similar results to be achieved.

Acknowledgment

This study was supported in part by MEXT Kakenhi Nos. 22103504 and 24103703.

5

EVALUATION OF COPD'S DIAPHRAGM MOTION EXTRACTED FROM 4D-MRI

Abstract

We have developed a method called intersection profile method to construct a 4D-MRI (3D+time) from time-series of 2D-MRI. The basic idea is to find the best matching of the intersection profile from the time series of 2D-MRI in sagittal plane (navigator slice) and time series of 2D-MRI in coronal plane (data slice). In this study, we use the reconstructed 4D-MRI to semi-automatically extract right diaphragm motion of 16 subjects (8 healthy volunteers and 8 COPD patients). The diaphragm motion is then evaluated quantitatively by calculating the displacement of each subjects and normalized it. We also generate inhalation phase length map to view and locate paradoxical motion of the COPD patients. The quantitative results of the normalized displacement shows that COPD patients tend to have smaller displacement compared to healthy volunteers. The average normalized displacement of total 8 COPD patients is 9.4mm and the average of normalized displacement of 8 healthy volunteers is 15.3mm. The generated phase-length maps show that not all of the COPD patients have paradoxical motion, however if it has paradoxical motion, the inhalation phase length map is able to locate where does it occur.

Keywords

4D-MRI, diaphragm motion, COPD, phase-length map.

5.1. Introduction

Chronic obstructive pulmonary disease (COPD) is a lung disorder characterized by airflow limitation that is irreversible [47]. The airflow limitation usually is a result of airway narrowing, parenchymal destruction or both [48]. Imaging modalities such as computed tomography (CT) can provide a visual assessment to observe structural imaging such as airways or lung parenchyma [48] [49] [50] [51].

Other imaging modality that is able to noninvasively quantify respiratory motion is magnetic resonance imaging (MRI) [52] [53] [54] [34] [28]. One of the advantage of the MRI over the CT imaging is that the MRI can obtain structural organ without irradiation. Using a fast acquisition techniques of MRI, Suga et al showed high spatial and temporal visualization of respiratory motion and also quantitatively evaluated the diaphragm motion of healthy volunteers and COPD [53]. Plathow et al used dynamic MRI to calculate vital capacity (VC) and compared it with VC calculated from spirometry. The correlation of VC calculated from spirometry and VC from dynamic MRI is high which indicates that MR imaging can be used to evaluate respiratory motion [54]. The use of dynamic MRI to investigate abnormal diaphragmatic motion on lung emphysema was also reported in [55]. Other study that evaluated the respiratory motion of lung parenchyma using dynamic MRI [28] was conducted by Shibata et al. Several points were set and tracked in ventrodorsal direction (X-axis) and craniocaudal direction (Y-axis). The tracking was only performed on a time-series sagittal slice. Therefore, the tracking points was limited in the anterior-posterior direction and unable to obtain respiratory motion in the right-left direction. Using only anterior-posterior tracking, the paradoxical motion of the diaphragm of COPD patients could not be confirmed.

Despite several studies have reported quantitative analysis of respiratory organs motion of COPD from dynamic MRI, a quantitative analysis from 4D imaging (3D + time) have never been reported. One of the advantages of 4D imaging over the dynamic MRI is that the anatomic motion and organ deformation caused by respiratory motion can be clearly observed in 3D which leads to better treatment [1] [2]. Some methods to reconstruct 4D imaging, specifically 4D-MRI include [8] [9] [10] [11] [12] [13]. A common approach to reconstruct 4D-MRI is using 2D-MR images to cover both the volume of the respiratory organ and the respiratory phases from inhalation to exhalation. The 2D-MR images are then retrospectively sorted based on the obtained respiratory phase to reconstruct the 4D-MR images (i.e. retrospective 4D-MRI).

In this study, we aim to obtain diaphragm motion from diaphragm surface that is extracted from 4D-MRI reconstructed using intersection profile method [13]. We then quantitatively analyze the differences of the diaphragm motion between the COPD patients and healthy volunteers.

In the following sections, we first review our method to reconstruct 4D-MRI and then we present the method of diaphragm motion extraction from 4D-MRI, displacement normalization and inhalation phase length (IPL) map generation. Finally, comparison of displacement and IPL map between COPD and healthy volunteers will be addressed.

5.2. Methods

5.2.1. Extraction of diaphragm motion from 4D-MRI

Our method to reconstruct 4D-MRI is discussed at Chapter 5, Sec. 5.2. In order to obtain diaphragm motion, we extract only on the right diaphragm motion. The left diaphragm is omitted because its motion are influenced by heart beat.

Four main steps to obtain diaphragm motion are: (1) set a region of interest (ROI) for the first frame; (2) set ROI for the subsequent frames; (3) track diaphragm surface for all frames (one respiratory cycle) based on the obtained ROI from (1) and (2); and (4) repeat the diaphragm surface tracking from anterior to posterior slice.

The ROI setting for the first frame is done manually by selecting 2-3 points at the surface of the diaphragm and connect them using interpolation (the selected points are not meant to represent the diaphragm surface but instead to be used as an initial contour for the next step). ROI is then set based on the lowest and highest location of the selected points. This ROI setting process is applied for each slices from anterior to posterior slice. Figure 5.1 shows the workflow of the ROI setting.

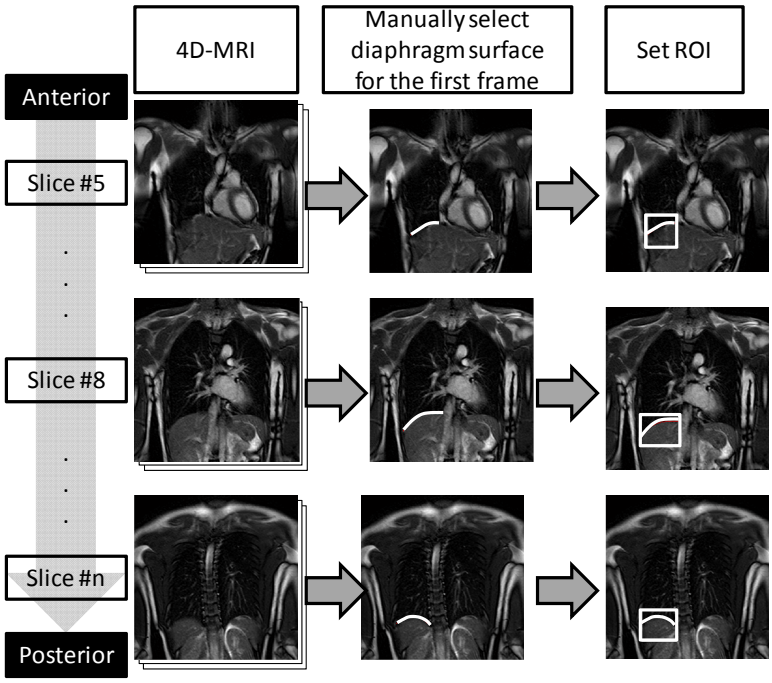

Figure 5. 1. Workflow of ROI setting for the first frame.

To automatically determine the ROI position for the subsequent frames, we use the ROI of the first frame as a template and find the best matching in the subsequent frames. The similarity measure we use to find the best matching is normalized cross correlation (NCC). Figure 5.1 shows the workflow to determine the ROI for one respiratory cycle (expiration-inspiration-expiration).

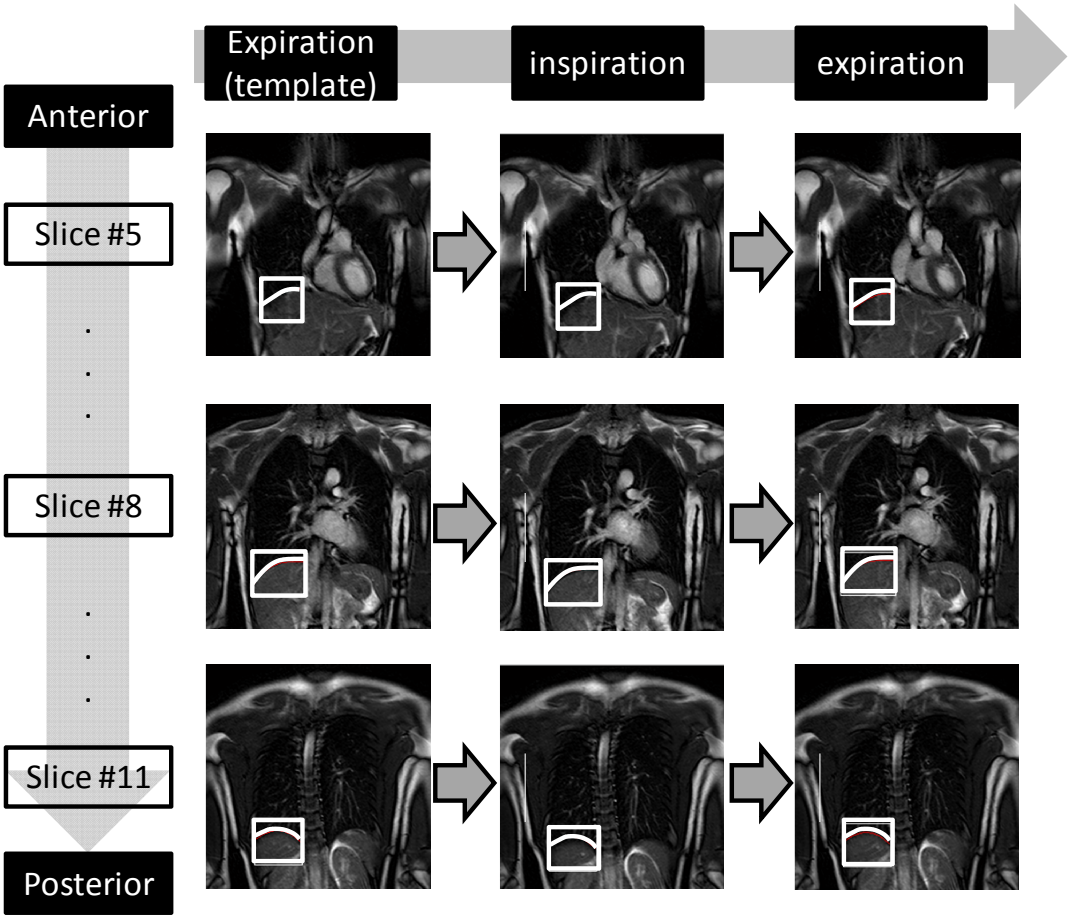

Figure 5. 2. ROI setting for the subsequent frames based on the template obtained from the first frame.

Next step is to track the diaphragm motion inside the ROI. This step is very crucial because it will be used to calculate the displacement and also generate phase-length map. The initial contour in step 1 cannot be used to represent the diaphragm surface because it just interpolates selected points in the diaphragm surface. There are many cases, especially for COPD subject where the shape of the diaphragm surface is not perfectly round or wavy. In such cases, the initial contour is unable to follow the wavy surface and more detail contour is required.

To obtain the detail contour for each frames, we first filter the ROI using Gaussian filtering to remove noise and apply active contour without edges method [36]. When

other parts besides the diaphragm surface are also detected, only the longest contour is considered as the diaphragm surface. Hence the final result is only one contour that represents the diaphragm surface on current frame and slice. Figure 5.3 shows how the active contour without edges is applied to obtain detail contour of the diaphragm surface.

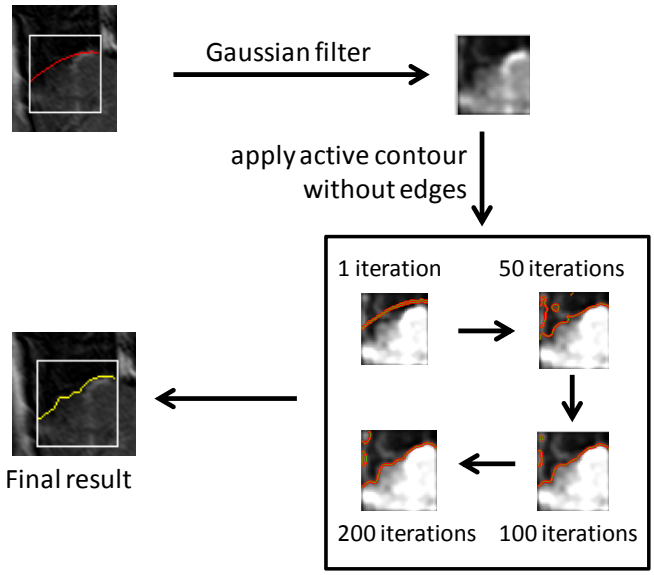

Figure 5. 3. Automatic detection of the diaphragm surface

This process of diaphragm surface detection is repeated for all subsequent frames (one respiratory cycle) and slices from anterior to posterior.

5.2.2. Normalization and IPL map

The displacement of the diaphragm is relative to subject's lung size. Therefore, normalized the displacement is necessary. We defined a normalized displacement as a percentage of diaphragm motion to the lung size. The displacement normalization (DN) is expressed as:

$$DN = (displ * 100) / d \qquad (5.1)$$

where *d* is length of the lung and *displ* is the difference point between end exhalation and end inhalation (Figure 5.4).

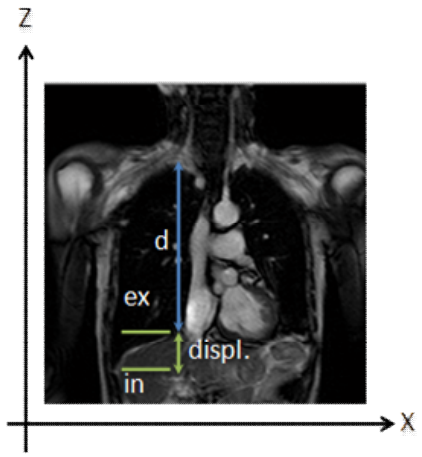

Figure 5. 4. Normalization of the displacement

The normalization is performed to each points in the contour of the diaphragm surface. Each points represents the displacement of the diaphragm from end-exhalation, end-inhalation and end-exhalation (one respiratory cycle). The displacement from end-exhalation to end-inhalation can be used to locate paradoxical motion of the diaphragm. Paradoxical motion is an abnormal chest movement that is considered as one of the characteristics of COPD in very severe stage. It is defined as downward (or upward) motion as lung area decreases (or increases) due to the poor airflow during respiration [55].

For healthy subjects, the lowest displacement (end-inhalation) falls between 30-40% in one respiratory cycle. However, for COPD patients there are parts of the diaphragm that moves asynchronously with the other parts. They move upward during inhalation and move downward during exhalation. Therefore, the lowest displacement for those parts falls between 70-80% in one respiratory cycle.

In order to locate paradoxical motion, we create a map called inhalation phase length (IPL) map. It maps the where is the lowest position (end-inhalation) of the displacement for each points. To determine the location of end-inhalation, we first extract displacement of diaphragm and normalized into 1-100 (where 1 represents the beginning of the respiratory cycle and 100 represents the end of the respiratory cycle). The end-inhalation is lowest position between 1-100. Figure 5.5 shows the detail to obtain IPL.

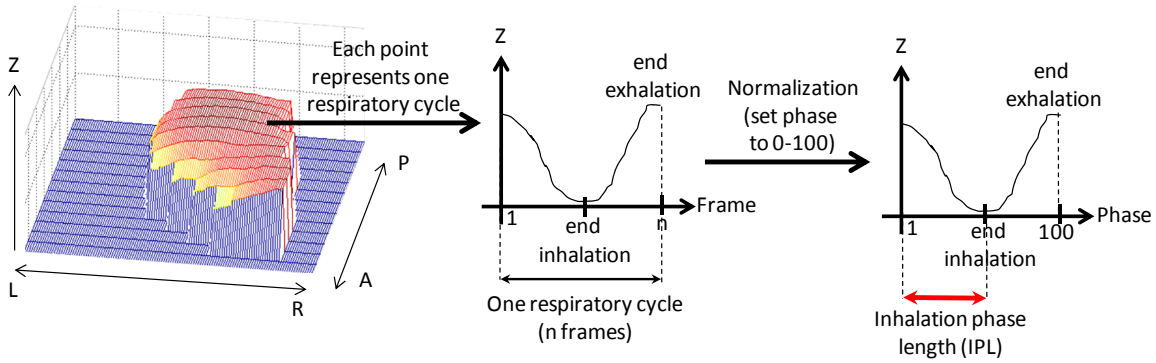

Figure 5. 5. Inhalation phase length (IPL) obtained from a point of displacement in the diaphragm

5.3 Experiment

5.3.1. Image data and patient characteristics used in experiment

The MR images were acquired using 1.5T INTERA ACHIVA nova-dual (Philips Medical Systems) whole-body scanner with a 16ch SENSE TORSO XL coil. A 2D balanced FFE sequence was used. The imaging parameters were as follows: SENSE factor, 2.2; flip angle, 45^{o}; TR, 2.2ms; TE, 0.9ms; FOV, 384mm; in-plane resolution, 256x256 pixels and 1.5x1.5mm^{2}; slice thickness, 7.5mm; slice gap, 6.0mm; scan time, 150ms/frame. All subjects were instructed to breath normally during the acquisition process. The image acquisition experiment was conducted under the approval of the Ethical Review Board of Chiba University. The software used to reconstruct 4D-MRI

was MatLab 7.10 and we ran it on a PC with Intel®Core™2 Quad, 2.66GHz, 16GB RAM.

The participant of this study were 8 COPD patients (6 men; mean age: 73±5.9 yr; mean height: 1.62±0.07 m; mean weight: 51±12kg) and 8 healthy volunteers (8 men; mean age: 32±1.4 yr; mean height: 1.76±4.38 m; mean weight: 67±5.6 kg) participated for this study. Detail of pulmonary function test (PFT) of COPD patients is shown in Table 5.1.

Table 5. 1. COPD patients characteristics

Pulmonary function test	**COPD patients**
Stage (GOLD standard)	
3	1
4	7
VC (l)	2.27±0.65
%VC	66.73±13.71
FVC (l)	2.17±0.71
%FVC	65.20±16.85
FEV1	0.73±0.32
FEV1/FVC	34.40±9.97
FEV1 % pred.	27.78±10.79

5.3.2. Diaphragm motion extraction and statistical analysis

Figure 5.6 shows the normalized displacement of COPD and healthy volunteers. As seen in the displacement map of COPD, most of the diaphragm area is blue or green which indicate the displacement is less than 10. For healthy volunteers, the displacement maps show some yellow or red area which indicate higher displacement.

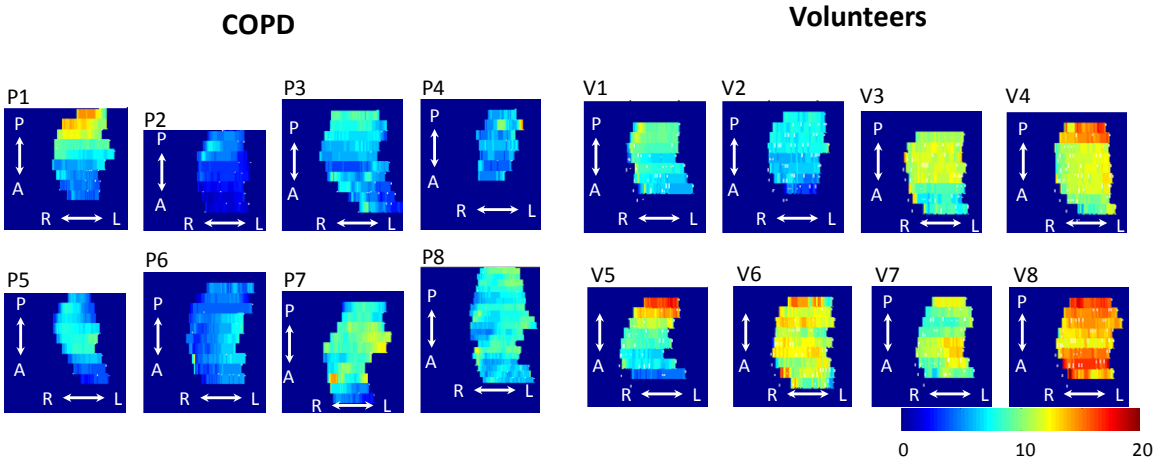

Figure 5. 6. Displacement map of COPD and healthy volunteers

Figure 5.7 shows the quantitative results of normalized displacement from COPD patients and healthy volunteers. The average of normalized displacement are 6.3±1.7 for COPD and 10.2±2.4 for healthy volunteers. We also performed a statistical analysis, t-test to see if the displacement of the COPD is significantly less than the healthy subjects. The p-value is equal to 0.000872, which indicate that the displacement of the COPD is significantly less than the volunteers

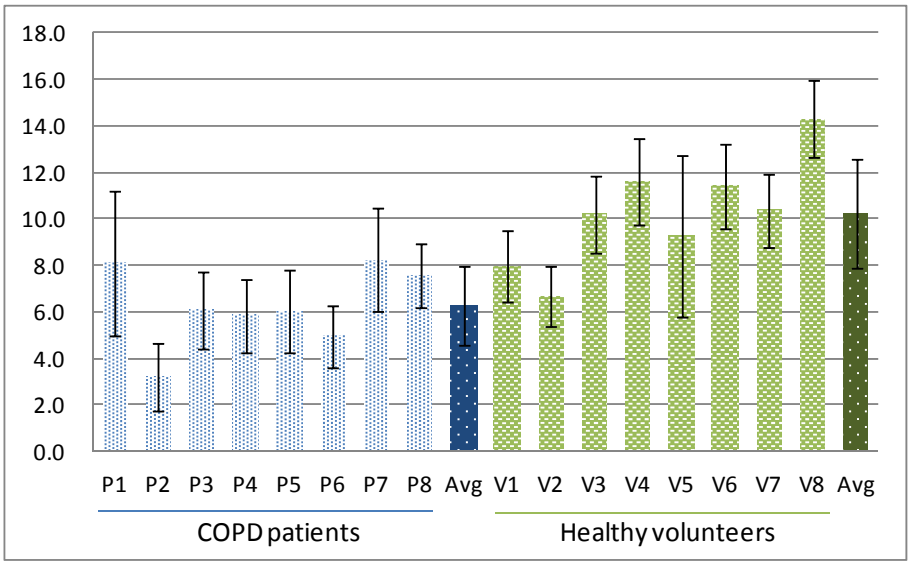

Figure 5. 7. Comparison of normalized displacement between COPD patients (P1-P8) and healthy volunteers (V1-V8)

5.3.3. Inhalation phase length (IPL) map

Figure 5.8 shows the IPL map of the COPD. Ideally, in one respiratory cycle, end-inhalation takes place somewhere between 30-40% (represented as green-yellow in the color bar). However, for certain area, the end of inhalation takes place at 60-70% (represented as red in the color bar) – which indicates paradoxical motion occur in that area.

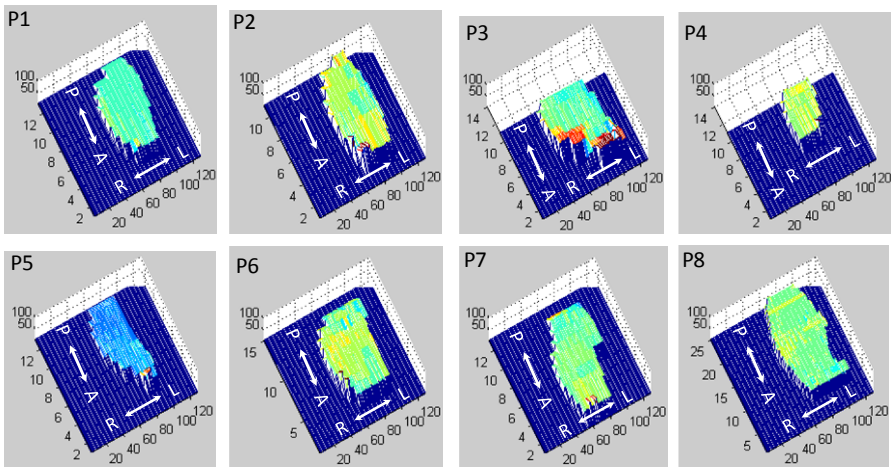

(a)

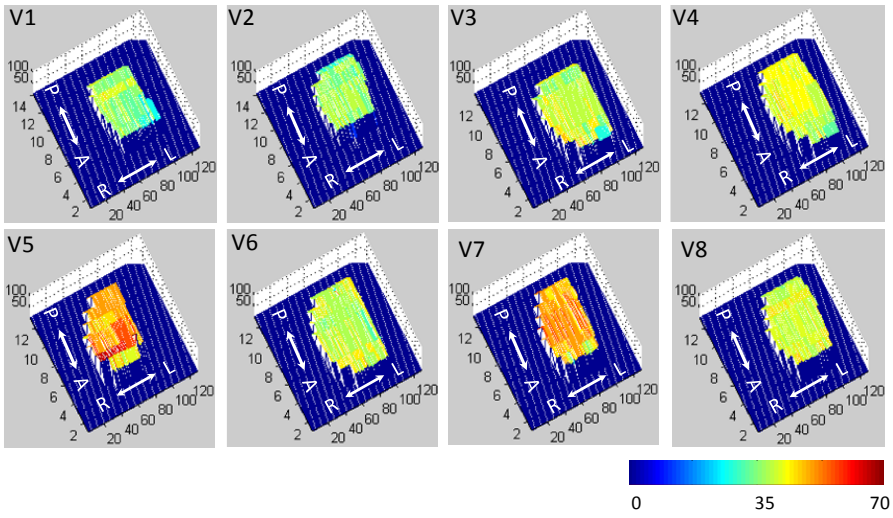

(b)

Figure 5. 8. IPLmap of (a) COPD and (b) healthy volunteers. The color bar represents the location of end inhalation (in %).

5.4 Discussion

We performed diaphragm motion extraction from 4D-MRI and calculate the normalized displacement of the diaphragm motion. The displacement of the COPD patients tend to have smaller displacement compared to healthy volunteers. This result confirms previous study by Shibata et al [28] that tracked several points in the lung during respiration and compared between COPD and healthy volunteers.

Using the extraction of the diaphragm motion, IPL map can be generated. An IPL map can be used to show the position of end-inhalation and also to locate paradoxical motion of the diaphragm. A very apparent paradoxical motion were shown in the IPL of P3. Our visual inspection of the diaphragm motion of P3 also showed that the red area moves asynchronously during respiration (Figure 5.9).

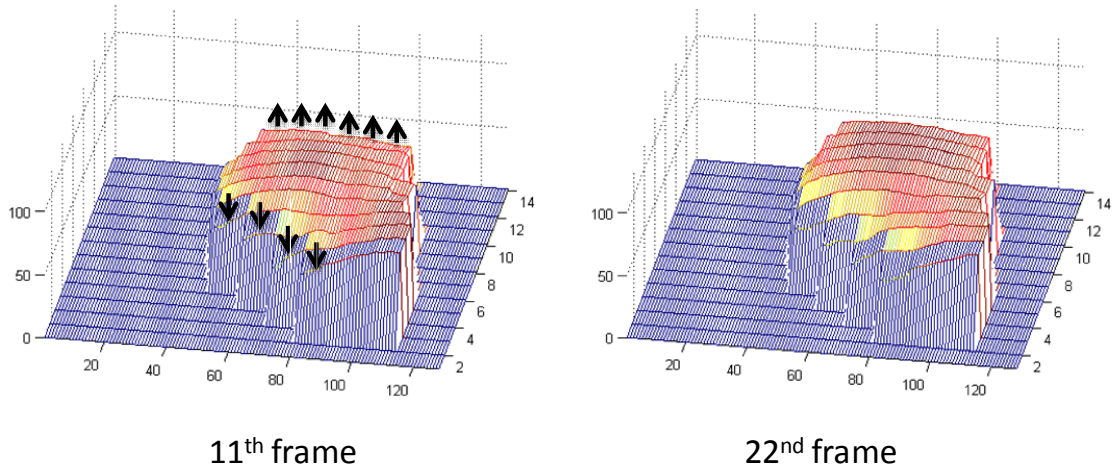

Figure 5. 9. Paradoxical motion of P3

Paradoxical motion also found in P2 and P5 in the right side near the anterior area. For P7, although there were small parts showing red, paradoxical motion could not be confirmed. The red parts only occur in two separate displacement points and caused by error during motion tracking process.

Two IPL maps of the volunteers, V5 and V7, showed that brown color dominates the diaphragm area. These cases were caused by the position of end-inhalation is higher compared to other volunteers. It cannot be categorized as paradoxical motion since most points of the end-inhalation position also falls in the 50%-60%.

5.5. Conclusion and future works

We extracted diaphragm motion from 4D-MRI of 8 COPD patients and 8 healthy volunteers. The displacement of the diaphragm were normalized and compared between COPD patients and healthy volunteers. The average of the normalized displacement of COPD patients are smaller compared to healthy volunteers. Using the same diaphragm motion, we also generated inhalation phase length map which can be used to locate paradoxical motion of the diaphragm, which is one of the characteristics of COPD.

The displacement of the diaphragm of COPD might have high correlation with the pulmonary functional tests. However, we need to confirm by adding more COPD data in the future.

Acknowledgment

This study was supported in part by MEXT Kakenhi Nos. 22103504 and 24103703

6

SUMMARY AND FUTURE WORKS

6.1. Summary

We present three aspects of 4D-MRI in this thesis: statistical modeling, reconstruction using prospective method and clinical application of 4D-MRI. The main contributions of each aspects are as follows:

- Statistical modeling using GND-PCA. Instead of using regular PCA, the GND-PCA provides better diaphragm motion modeling which has smaller error margin.
- Reduction of acquisition time using prospective method to reconstruct 4D-MRI. Our proposed method is able to reduce the acquisition time of data slice up to 75% while maintaining the quality of the reconstruction. Although full-scale implementation of this method is currently not possible, we believe that upon implementation, it is reasonable to expect similar time acquisition reduction.
- Application of 4D-MRI to locate paradoxical motion in the diaphragm of the COPD patients.

6.2. Future works

In chapter 2, we proposed diaphragm motion modeling using GND-PCA. The subjects in the diaphragm motion modeling are healthy subjects. We did not include patient in the sample. It is interesting if several patients with paradoxical motion are

also included in the sample. Since PCA captures the largest possible variance of motion, we can expect that the paradoxical motion is also captured in the PCA model. However, an experiment is required to support the hypothesis. The motion model can also be used along with surrogate data that have a strong relationship with the motion of interest to estimate motion of interest. It opens new potential for clinical applications such as image guided intervention or more accurate treatment for radiotherapy.

In chapter 4, we discussed the improvement of 4D-MRI reconstruction method. The current method is only able to capture 1 most common respiratory cycle. It is interesting if the variability of the respiratory cycles can be obtained. The analysis of respiratory motion or respiratory modeling will be more accurate if the 4D-MRI can capture respiratory cycle variability.

In clinical application, there are still many potentials of 4D-MRI that can be explored in the future. We have proposed a method to extract the diaphragm motion and quantitatively analyzed the displacement in chapter 5. We showed that the normalized displacement of the COPD tend to be smaller compared to the healthy volunteer. Other application is measuring the change of lung volume of COPD. It will benefit the physicians to have more understanding of COPD and its relationship with the severity of COPD. The correlation of paradoxical motion and airflow obstruction is also another interesting topic that can be investigated using 4D-MRI.

BIBLIOGRAPHY

[1] P. J. Keall, G. S. Mageras and J. M. Balter, "The management of respiratory motion in radiation oncology report of AAPM Task Group 76a," *Medical physics,* vol. 33, no. 10, pp. 3874-3900, 2006.

[2] P. Keall, "4-dimensional computed tomography imaging and treatment planning," *Seminars in radiation oncology ,* vol. 14, no. 1, pp. 81-90, 2004.

[3] S. S. Vedam, P. J. Keall, V. Kini and a. et, "Acquiring a four-dimensional computed tomography dataset using an external respiratory signal," *Physics in medicine and biology,* vol. 48, no. 1, p. 45, 2003.

[4] K. Saito, M. Saito, S. Komatu and a. et, "Real-time four-dimensional imaging of the heart with multi-detector row CT," *Radiographics,* vol. 23, no. 1, pp. E8-E8, 2003.

[5] D. A. Low, M. Nystrom, E. Kalinin and a. et, "A method for the reconstruction of four-dimensional synchronized CT scans acquired during free breathing," *Medical physics,* vol. 30, no. 6, pp. 1254-1263, 2003.

[6] R. W. Underberg, F. J. Lagerwaard, J. P. Cuijpers and a. et, "Four-dimensional CT scans for treat-ment planning in stereotactic radiotherapy for stage I lung cancer," *Journal of Radiation Oncology* Biology* Physics,* vol. 60, no. 4, pp. 1283-1290, 2004.

[7] W. Lu, P. J. Parikh, I. M. El Naqa and a. et, "Quantitation of the reconstruction quality of a four-dimensional computed tomography process for lung cancer patients," *Medical physics,* vol. 32, no. 4, pp. 890-901, 2005.

[8] M. von Siebenthal, G. Székely, U. Gamper and a. et, "4D MR imaging of respiratory organ motion and its variability," *Phys Med Biol,* vol. 52, p. 1547–1564, 2007.

[9] J. Tokuda, S. Morikawa, H. Haque and a. et, "Adaptive 4D MR imaging using navigator-based respiratory signal for MRI-guided therapy," *Magn Reson Med.,* vol. 59, no. 5, pp. 1051-1061, 2008.

[10] G. Remmert, J. Biederer, F. Lohberger and a. et, "Four-dimensional magnetic resonance imaging for the determination of tumour movement and its evaluation using a dynamic porcine lung phantom," *Physics in medicine and biology,* vol. 52, no. 18, p. N401, 2007.

[11] J. Cai, C. Z, Z. Wang and a. et, "Four-dimensional magnetic resonance imaging (4D-MRI) using image-based respiratory surrogate: a feasibility study," *Medical physics,* vol. 38, no. 12, pp. 6384-6394, 2011.

[12] A. P. King, C. Buerger, C. Tsoumpas and a. et, "Thoracic respiratory motion estimation from MRI using a statistical model and a 2-D image navigator," *Medical image analysis,* vol. 16, no. 1, pp. 252-264, 2012.

[13] Y. Masuda and H. Haneishi, "4D MR Imaging of Respiratory Organ Motion using Intersection Profile Method," *Proc of SPIE ,* vol. 7625, pp. 76250Z-1-76250Z-10, 2010.

[14] R. Werner, J. Ehrhardt, T. Frenzel and a. et, "Motion Artifact Reducing

Reconstruction of 4D CT Image Data for the Analysis of Respiratory Dynamics," *Meth. Inf. Med.,* vol. 46, pp. 254-260, 2007.

[15] R. Werner, J. Ehrhardt, R. Schmidt and H. Handels, "Modeling respiratory lung motion: a biophysical approach using finite element methods.," *Proc. SPIE,* vol. 6916, pp. N1-11, 2008.

[16] J. McClelland, J. Blackall and S. Tarte, "A continuous 4D motion model from multiple respiratory cycles for use in lung radiotherapy," *Medical Physics,* no. 33, pp. 3348-3358, 2006.

[17] M. Georg, R. Souvenir, A. Hope and R. Pless, "Manifold learning for 4D CT reconstruction of the lung.," *Computer Vision and Pattern Recognition Workshops,* vol. 2008, no. CVPRW08, pp. 1-8.

[18] M. Lyksborg, R. Paulsen, C. Brink and R. Larsen, "4D Lung Reconstruction with Phase Optimization," *IFMBE Proceedings,* pp. 2227-2230, 2010.

[19] R. Li, J. Lewis, X. Jia, T. Zhao and a. et, "PCA-based lung motion model," *16th International Conference on the Use of Computers in Radiation Therapy,* 2010.

[20] T. Klinder, C. Lorenz and C. Ostermann, "Free-breathing intra-and inter-subject respiratory motion capturing, modeling, and prediction," *Proc. SPIE,* vol. 7259, p. 72590T, 2009.

[21] P. King, C. Buerger and T. Schaeffter, "Cardiac respiratory motion modelling by simultaneous registration and modelling from dynamic MRI images," *Biomedical Image Registration,* vol. 4th International Workshop, pp. 222-233, 2010.

[22] W. Wein, J.-Z. Cheng and A. Khamene, "Ultrasound based respiratory motion compensation in the abdomen.," *MICCAI 2008 Worshop on Image Guidance and*

Computer Assistance for Softissue Intervetions, vol. 32, no. 6, p. 294, 2008.

[23] R. Xu and Y. W. Chen, "Generalized N-dimensional principal component analysis (GND-PCA) and its application on construction of statistical appearance models for medical volumes with fewer samples," *Neurocomputing,* vol. 72, no. 10, pp. 2276-2287, 2009.

[24] S. J. McQuaid, T. Lambrou, V. Cunningham and a. et, "The application of a statistical shape model to diaphragm tracking in respiratory-gated cardiac pet images," *Proceedings of the IEEE,* vol. 97, no. 12, pp. 2039-2052, 2009.

[25] T. F. Cootes, C. J. Taylor, D. H. Cooper and J. Graham, "Active shape models-their training and application," *Computer vision and image understanding,* vol. 61, no. 1, pp. 38-59, 1995.

[26] Z. Qiu, H. Tang and D. Tian, "Non-rigid medical image registration based on the thin-plate spline algorithm," *Computer Science and Information Engineering,* vol. 2, pp. 522-577, 2009.

[27] S. J. Martin, J. Dey, M. A. King and B. F. Hutton, "Segmenting and Tracking Diaphragm and Heart Regions in Gated-CT Datasets as an Aid to Developing a Predictive Model for Respiratory Motion-Correction," *Nuclear Science Symposium Conference Record,* vol. 4, pp. 2680-2685, 2007.

[28] H. Shibata, T. Iwasawa, T. Gotoh and a. et, "Automatic Tracking of the Respiratory Motion of Lung Parenchyma on Dynamic Magnetic Resonance Imaging: Comparison With Pulmonary Function Tests in Patients With Chronic Obstructive Pulmonary Disease," *Journal of thoracic imaging,* vol. 27, no. 6, pp. 387-392, 2012.

[29] M. J. Diament, M. I. Boechat and H. Kangarloo, "Real‐time sector ultrasound in the evaluation of suspected abnormalities of diaphragmatic motion," *Journal of clinical ultrasound,* vol. 13, no. 8, pp. 539-543, 1985.

[30] E. O. Gerscovich, M. Cronan, J. McGahan and a. et, "Ultrasonographic evaluation of diaphragmatic motion," *Journal of ultrasound in medicine,* vol. 20, no. 6, pp. 597-604, 2001.

[31] A. Boussuges, Y. Gole and P. Blanc, "Diaphragmatic motion studied by m-mode ultrasonography," *Chest,* vol. 135, no. 2, pp. 391-400, 2009.

[32] T. Kotani, S. Minami, K. Takahashi and a. et, "An analysis of chest wall and diaphragm motions in patients with idiopathic scoliosis using dynamic breathing MRI," *Spine,* vol. 29, no. 3, pp. 298-302, 2004.

[33] P. Kolar, J. Neuwirth, Sanda and a. et, "Analysis of diaphragm movement during tidal breathing and during its activation while breath holding using MRI synchronized with spirometry," *Physiological Research,* vol. 58, no. 3, p. 383, 2009.

[34] T. Iwasawa, H. Takahashi, T. Ogura and a. et, "Influence of the distribution of emphysema on diaphragmatic motion in patients with chronic obstructive pulmonary disease," *Japanese journal of radiology,* vol. 29, no. 4, pp. 256-264, 2011.

[35] N. Otsu, "A threshold selection method from gray-level histograms," *Automatica,* vol. 11, no. 285-296, pp. 23-27, 1975.

[36] T. F. Chan and L. A. Vese, "Active contours without edges," *Image Processing, IEEE Transactions on,* vol. 10, no. 2, pp. 266-277, 2001.

[37] W. Lu, M. M. Nystrom, P. J. Parikh and a. et, "A semi-automatic method for peak and valley detection in free-breathing respiratory waveforms," *Medical physics,* vol. 33, no. 10, pp. 3634-3636, 2006.

[38] R. C. Gonzalez, R. E. Woods and S. L. Eddins, Digital Image Processing using MATLAB, Prentince Hall, 2004.

[39] Z. Wang, A. C. Bovik, H. R. Sheikh and a. et, "Image quality assessment: from error visibility to structural similarity," *Image Processing, IEEE Transactions on,* vol. 13, no. 4, pp. 600-612, 2004.

[40] D. M. Rouse and S. S. Hemami, "Understanding and simplifying the structural similarity metric," in *15th IEEE International Conference In Image Processing*, 2008.

[41] Z. Liu and R. Laganiere, "On the Use of Phase Congruency to Evaluate Image Similarity," in *ICASSP (2)*, 2006.

[42] H. Alain and D. Ziou, "Is there a relationship between peak-signal-to-noise ratio and structural similarity index measure?," *Image Processing,* vol. 7, no. 1, pp. 12-24, 2013.

[43] K. Bijendra, S. B. Kumar and C. Kumar, "Development of improved SSIM quality index for compressed medical images," in *Image Information Processing (ICIIP)*, 2013.

[44] Z. Zangen, K. Wahid, P. Babyn and R. Yang, "Compressed sensing-based MRI reconstruction using complex double-density dual-tree DWT," *Journal of Biomedical Imaging,* p. 10, 2013.

[45] A. Betgen, A. Tanja, S. Jan-Jakob, V. Corine van, B. Harry and R. Peter,

"Assessment of set-up variability during deep inspiration breath hold radiotherapy for breast cancer patients by 3D-surface imaging," *Radiotherapy and Oncology ,* vol. 2, pp. 225-230, 2013.

[46] W. Swastika, Y. Masuda, N. Kawata, K. Matsumoto, T. Suzuki, K. Iesato, Y. Tada, T. Sugiura, N. Tanabe, K. Tatsumi, T. Ohnishi and H. Haneishi, "Evaluation of COPD's diaphragm motion extracted from 4D-MRI," in *SPIE*, Florida, 2015.

[47] B. R. Celli, W. MacNee, A. Agusti and a. et, "Standards for the diagnosis and treatment of patients with COPD: a summary of the ATS/ERS position paper," *European Respiratory Journal,* vol. 23, no. 6, pp. 932-946, 2004.

[48] M. Hasegawa, Y. Nasuhara, Y. Onodera and a. et, "Airflow limitation and airway dimensions in chronic obstructive pulmonary disease.," *American journal of respiratory and critical care medicine,* vol. 173, no. 12, pp. 1309-1315, 2006.

[49] A. Haruna, S. Muro, Y. Nakano and a. et, "CT scan findings of emphysema predict mortality in COPD," *CHEST,* vol. 138, no. 3, pp. 635-640, 2010.

[50] Barr and e. a. COPDGene CT Workshop Group: R. Graham, "A combined pulmonary-radiology workshop for visual evaluation of COPD: study design, chest CT findings and concordance with quantitative evaluation.," *COPD: Journal of Chronic Obstructive Pulmonary Disease,* vol. 9.2, pp. 151-159, 2012.

[51] T. Ohara, T. Hirai, S. Muro and a. et, "Relationship between pulmonary emphysema and osteoporosis assessed by CT in patients with COPD," *CHEST,* vol. 134, no. 6, pp. 1244-1249, 2008.

[52] J. Tokuda, M. Schmitt, Y. Sun and a. et, "Lung motion and volume measurement by dynamic 3D MRI using a 128-channel receiver coil," *Academic Radiology,* vol.

16, no. 1, pp. 22-27, 2009.

[53] K. Suga, T. Tsukuda, H. Awaya and a. et, "Impaired respiratory mechanics in pulmonary emphysema: evaluation with dynamic breathing MRI," *Journal of Magnetic Resonance Imaging,* vol. 10, no. 4, pp. 510-520, 1999.

[54] C. Plathow, M. Schoebonger, C. Fink and a. et, "Evaluation of lung volumetry using dynamic three-dimensional magnetic resonance imaging," *Investigative radiology,* vol. 40, no. 3, pp. 173-179, 2005.

[55] T. Iwasawa, S. Kagei, T. Gotoh and a. et, "Magnetic resonance analysis of abnormal diaphragmatic motion in patients with emphysema," *European Respiratory Journal,* vol. 19, no. 2, pp. 225-231, 2002.

[56] M. Schneider and a. et, "Model-based respiratory motion compensation for image-guided cardiac interventions," *Computer Vision and Pattern Recognition (CVPR),* pp. 2948-2954, 2010.

[57] K. Demura, S. Morikawa, K. Murakami and a. et, "An easy-to-use microwave hyperthermia system combined with spatially resolved MR temperature maps: phantom and animal studies," *Journal of Surgical Research,* vol. 135, no. 1, pp. 179-186, 2006.

[58] S. C. Bushong, Magnetic Resonance Imaging: Physical and Biological Principles, Mosby, 2003.

[59] C. Westbrook, Handbook of MRI Technique, Wiley-Blackwell, 1999.

[60] W. Hendee and R. Ritenour, Medical imaging physics, John Wiley & Sons, 2003.

RELEVANT PUBLICATIONS BY THE AUTHOR

Articles in International Journals

1. Windra Swastika, Yoshitada Masuda, Takashi Ohnishi and Hideaki Haneishi: "Reduction of acquisition time in the intersection profile method for four-dimensional magnetic resonance imaging reconstruction of thoracoabdominal organs," J. Med. Imag., 2(2), 024008, 14 pages (2015). doi:10.1117/1.JMI.2.2.024008
2. Windra Swastika, Yoshitada Masuda Takashi Ohnishi and Hideaki Haneishi: "Automatic Extraction of Diaphragm Motion and Respiratory Pattern from Time-sequential Thoracic MRI", TELKOMNIKA, Vol.14, No.2, pp. 329-334 (2015.5)
3. Windra Swastika, Yoshitada Masuda, Rui Xu, Shoji Kido, Yen-Wei Chen, and Hideaki Haneishi, "GND-PCA-Based Statistical Modeling of Diaphragm Motion Extracted from 4D MRI," Computational and Mathematical Methods in Medicine, vol. 2013, Article ID 482941, 9 pages, (2013). doi:10.1155/2013/482941
4. Windra Swastika, Hideaki Haneishi: Compressed Sensing for Thoracic MRI with Partial Random Circulant Matrices, TELKOMNIKA, Vol.10, No.1, pp. 147-154 (2012.3)

Articles in International Conferences with Review Committee

1. Windra Swastika, Yoshitada Masuda, Naoko Kawata, Koji Matsumoto, Toshio Suzuki, Ken Iesato, Yuji Tada, Toshihiko Sugiura, Nobuhiro Tanabe, Koichiro Tatsumi, Takashi Ohnishi, Hideaki Haneishi, "Evaluation of COPD's diaphragm motion extracted from 4D-MRI", SPIE Medical Imaging, Florida, USA, (Feb 21-26, 2015)

2. Windra Swastika, Yoshitada Masuda, Takashi Ohnishi, Hideaki Haneishi, "Time Reduction of 4D-MRI Reconstruction for Thoracoabdominal Organs using Intersection Profile Method", CARS 28th International Congress and Exhibition, Fukuoka, Japan, (Jun 24-28, 2014)

3. Swastika W, Masuda Y, Xu R, Kido S, Chen YW, Haneishi H, "Statistical Modeling of Diaphragm Motion Extracted from 4D-MRI using 1DPCA and 2DPCA". Proc. of International Forum on Medical Imaging in Asia (IFMIA), Korea, (Nov 16-17, 2012)

4. Swastika W, Nishikawa T, Masuda Y, Haneishi H, "Statistical Model of Diaphragm Motion Using Principal Component Analysis". Proc of 97th Radiology Society of North America (RSNA) scientific assembly and annual meeting, Chicago, USA, 2011.

Abstract in Other Conferences

1. Swastika W, Nishikawa T, Masuda Y, Haneishi H, "Statistical Model of Diaphragm Motion Using Principal Component Analysis". Proc of 30th Japanese Society of Medical Imaging Technology (JAMIT) annual meeting, Otawa, Japan, 2011

2. Windra Swastika, Yoshitada Masuda, Hideaki Haneishi, "Automatic Intersection Profile Method for 4D-MRI Construction". 5th Japanese Society of Pulmonary Functional Imaging (JSPFI) 2013, P11-5, Tokushima, (Jan 12-13, 2013)

3. Windra Swastika, Yoshitada Masuda, Hideaki Haneishi, "Automation and Time Reduction of 4D-MRI Reconstruction for Thoracoabdominal Organs using Intersection Profile Method", 第 32 回 日本医用画像工学会大会，PP2-6,産業技術総合研究所臨海副都心センター(2013.8.1-3)

4. Windra Swastika, Yoshitada Masuda, Naoko Kawata, Koji Matsumoto, Toshio Suzuki, Ken Iesato, Yuji Tada, Tanabe Sugiura, Nobuhiro Tanabe, Koichiro Tatsumi, Takashi Ohnishi, Hideaki Haneishi: Visual and quantitative assessment of COPD's diaphragm motion extracted from 4D-MRI, 第 6 回 呼吸機能イメージング研究会 2013, P-74, 北海道大学, (2014.01.23-24)

ACKNOWLEDGEMENT

Doctoral course is an amazing and yet challenging journey. Without help from many people, I could never have reached the end point of this journey.

First, I want to express my gratitude to my supervisor Prof. Hideaki Haneishi for many things. For accepting me to join his laboratory back then in 2010. For giving me a freedom to do research and also directing my research topic in the same time. For giving me so many valuable insights from the beginning of my research and all the way to final thesis defense. All of those experiences are priceless.

I would to thank Takashi Ohnishi as a senior and co-supervisor as well. He was there to help me familiarize with the lab. environment, setting up the PC, network and software I used on my first days in the laboratory. I really appreciate his kindness and could not ask for more.

I would also to thank Prof. Etsuji Yamamoto, Prof. Wenwei Yu and Prof. Tadashi Yamaguchi for their advices and suggestions. Their advices and suggestions has helped this thesis to reach a better scientific writing.

Finally, I would like to thank my wife, Theresia and my children, Hide-kun and Megu-chan. Thank you for the love, support and encouragement during my doctoral journey.